Physics – Uspekhi **60** (1) 40 – 57 (2017)

REVIEWS OF TOPICAL PROBLEMS

PACS numbers: 13.85.Tp, **14.60. – z**, **29.30. – h**, 75.50.Ww, **95.30. – k**, **95.55. – n**, 96.50.S – , **97.60. – s**, 98.58.Mj, 98.70.Sa

Search for antimatter and dark matter and precision studies of cosmic ray fluxes on the International Space Station. AMS experiment. Results of four-year exposure

Yu V Galaktionov

DOI: https://doi.org/10.3367/UFNe.2016.03.037764

Contents

Abstract. The results of cosmic rays studies obtained in the AMS experiment in 2011–2015 on the International Space Station are discussed. Research on the energy spectra of electrons and positrons at TeV energies and precision measurements of fluxes were performed. The growth of the positron fraction with energy was observed. Proton and helium spectra were also obtained. A review of theoretical models with possible explanations of the observed phenomena is presented.

Keywords: outer space, orbit, experiment, cosmic rays, positrons, dark matter, protons, experimental setup, high energy

1. Introduction

The studies in this paper are on the borderline of the areas covered by elementary particle physics and astrophysics, both experiencing fast development over recent decades. Experimental physics has reached the level where theoretical ideas about the 'beginning of the Universe' can undergo experimental verification. We can try, for example, to verify whether elementary particle interaction laws and symmetry laws that are valid now and in our part of the Universe were also valid in the Early Universe right after the Big Bang. We can attempt to see if the consequences of fundamental laws acting in the micro world are in accordance with astrophysical observations.

In 1994, on the initiative of Samuel Ting of MIT, a group of physicists from a number of universities in Switzerland, Germany, Russia, Italy, France, the USA, Spain, Portugal, China, and Taiwan proposed a program to perform an elementary particle physics experiment on the International Space Station (ISS), then under construction. The program was named Alpha Magnetic Spectrometer (AMS), and it has continued for more than twenty years [1].

The idea of the experiment is simple: our Earth is surrounded by a material, an atmosphere, 1 kg m^{-2} thick, and therefore charged particles reach Earth's surface considerably weakened and accompanied by multiple interaction products. Cosmological experiments are therefore performed exclusively with electromagnetic radiation, and to work with charged cosmic ray particles, we should go beyond the atmosphere.

An orbital magnetic spectrometer is intended for cosmological studies.

We briefly discuss the basic ideas that have led to the theory of the expanding Universe. In Newton's time, the Universe was considered static, and to avoid obvious gravitational collapse, Newton introduced an infinite number of galaxies. Einstein presented a more realistic picture: he introduced a so-called 'cosmological term', that is, some additional repulsion of big masses. The observation of 'red shift', as well as more reliable measurements of the distances to far galaxies led to Friedmann's picture of galaxies 'running away' and, consequently, to the expanding Universe. This allowed Hubble to formulate his famous law: velocities of galaxies are proportional to the distances to them. The coefficient of proportionality, known as the 'Hubble con-

Yu V Galaktionov. Massachusetts Institute of Technology (MIT), 77 Massachusetts Ave, Cambridge, MA 02139, USA
E-mail: iouri.galaktionov@cern.ch

Received 3 February 2016, revised 20 March 2016
Uspekhi Fizicheskikh Nauk **187** (1) 45 – 64 (2017)
DOI: https://doi.org/10.3367/UFNr.2016.03.037764
Translated by Yu V Galaktionov; edited by A M Semikhatov

stant', is not in reality a constant and, according to general relativity, is time dependent. If we look at the Universe on a large enough scale, its expansion originates from isotropy and homogeneity, observed with great accuracy. The most general form of the metric corresponding to an isotropic and homogeneous space contains a scale factor R that is responsible for the evolution of the coordinate scale with time. The increase in R with time leads to the expansion of the Universe.

In the course of expansion, there comes a moment when radiation ceases to interact with matter, neutral atoms are formed, and free electrons disappear, but photons stay. This happens when the temperature of the Universe drops to 4000 K. The spectrum of those relic photons is a black-body spectrum with the temperature corresponding to the moment when free electrons disappeared. The spectrum then underwent a red shift in accordance with the rate and time of the expansion of the Universe. The frequencies have shifted proportionally to R; therefore, the relic radiation spectrum turns out to correspond to the temperature of around 5 K, and direct measurements of the spectrum shape give 2.7 K. This provides excellent confirmation of the Big Bang theory.

Yet one more observation confirms the Big Bang theory. This is the abundance in the Universe of the elements ^{4}He, ^{3}He, ^{2}D, and ^{7}Li, which originate from nuclear reactions in the early Universe. The observed values are close to theoretical predictions.

A number of problems with the Big Bang theory — the fact that space is Euclidean with extreme accuracy (10^{-15}) in the early Universe and the causality problem (different parts of Universe are at the same temperature, although signal exchange between them is impossible) — are solved through the introduction of inflation.

1.1 Search for antinuclei

One of the problems with the Big Bang theory is the baryon asymmetry. Being produced in equal numbers, baryons and antibaryons quickly annihilate in the course of expansion and cooling of the Universe and finally some part of the baryons is retained, whereas antibaryons totally disappear in the observable part of the Universe. There are a number of theories explaining the baryon asymmetry, but they have not been subjected to experimental verification [3].

Antimatter could be detected experimentally due to the following effects.

(1) The existence of an irregularity in the spectrum of energetic gamma rays arising in processes of baryon annihilation. The irregularity should appear in the MeV part of the gamma-ray spectrum originating from the decay of neutral mesons produced by the baryon–antibaryon pair annihilation.

(2) The search for antinuclei in cosmic rays. The observation of antinuclei of helium or heavier elements would be direct proof of the existence of antimatter. However, the antinuclei can be deflected by magnetic fields existing in the interstellar space, intergalactic space, the space between clusters of galaxies or between clusters of clusters of galaxies, etc.

The interpretation of negative searches therefore becomes dependent on our knowledge of the magnetic fields in the Universe. Unfortunately, modern means of observing cosmological magnetic fields are not sensitive enough.

1.2 Search for dark matter

A number of astrophysical observations show that most of matter in the Universe does not radiate and is therefore unseen by modern detection techniques. The manifestations are numerous:

(1) rotation curves of spiral galaxies;

(2) orbital velocities of galaxies inside clusters being an order of magnitude above expectations;

(3) gravitational lensing;

(4) fluctuations of cosmic microwave background radiation being two orders of magnitude above expectations;

(5) the density of observed matter being two orders of magnitude below critical;

(6) large-scale structures;

(7) the abundance of light elements corresponding to a low density of visible matter [4].

What particles constitute dark matter is unknown. There are many hypotheses, for example, the neutralino is the dark matter particle in the SUSY approach. The interactions of neutralinos in the Galaxy produce $\bar{\mathrm{p}}$, e^+, and γ:

$$\begin{aligned}\chi + \chi &\to \bar{\mathrm{p}} + \dots ,\\ &\to \mathrm{e}^+ + \dots ,\\ &\to \gamma + \dots .\end{aligned}$$

Naturally, the spectra of $\bar{\mathrm{p}}$, e^+, and γ thus produced would be different from the spectra originating from ordinary matter, and precision measurements must show whether the neutralino is a dark matter particle.

The manifestation of dark matter particles in any of the channels (e^+, e^-, $\bar{\mathrm{p}}$, ...) will not by itself be sufficient to identify the nature of dark matter. Collider experiments will be able to identify long-lived weakly interacting particles but without a connection to cosmology. Only by combining different approaches can the dark matter mystery be resolved.

1.3 Cosmic ray spectra

Measurements of the electromagnetic part of the cosmic-ray spectrum (the cosmic microwave background radiation, X-rays, and gamma rays) performed in the last 50 years have been at the origin of many Nobel prizes: the discoveries include pulsars, the cosmic microwave background radiation and its anisotropy, a new type of pulsars, and X-ray sources.

Due to the long duration of measurement and the large solid angle, AMS measurements of cosmic-ray spectra have reached an unprecedented level of accuracy: before the AMS, the typical measurement accuracy was 30–40%, but the AMS data are accurate to 1% or less. The AMS collects a very large statistics not solely for protons, electrons, and helium; extremely precise spectrum measurements have been obtained for B, C, Li, and many other elements, not to mention very high energies that had been unavailable previously. These measurements are of fundamental importance to understand the origin and propagation of cosmic rays.

2. AMS detector

The Alpha Magnetic Spectrometer [5, 6] is intended to measure high-energy particle spectra with a high statistics, obtained by the long duration of the experiment, thus ensuring the statistics two or three orders of magnitude greater than in the 'standard' cosmic-ray measurements. When designing the AMS, we profited from the considerable past experience of the successful performance of many high-energy physics experiments on accelerators.

The following principal considerations led to the success of experiments.

(a) Minimal amount of material in the way of particles. The material should not become a source of the background and should not noticeably increase the number of large-angle scattering events.

(b) Multiple momentum and velocity measurements to avoid the background from particles that have undergone large-angle scattering in detector material with the risk of mixing with the signal.

The AMS composition now working on board the ISS consists of the following elements (Fig. 1) [6]:

(1) A 20-layer transition radiation detector (TRD) identifies electrons and positrons with the proton background suppressed by a factor of 1000 at 1.5 GeV and 100 at 300 GeV.

(2) Four layers of time-of-flight (TOF) counters with an accuracy of 160 ps also serve to make ionization measurements.

(3) Nine layers of silicon detectors in a permanent magnet ensure measurements of momentum (rigidity) of particles.

(4) Anticoincidence counters detect only particles that pass through the magnet aperture.

(5) A RICH Cherenkov counter measures the velocity (with a 0.1% accuracy) and charge of particles and nuclei. By combining these measurements with the momentum measured in the tracker, the particle mass can be identified.

(6) A three-dimensional ECAL calorimeter, made of lead plates interspersed with scintillation fiber layers for a total thickness of 16.7 rad. lengths measures the energy of gamma rays, electrons, and positrons. ECAL identifies the electrons and positrons, suppressing protons by a factor of 10^4 in the energy range from 1.5 to several hundred GeV.

The electric charge is measured independently by a coordinate detector (Tracker), a RICH counter, and TOF counters. The sign of the charge ($\pm Z$) and momentum (P) are measured by the trajectory in the magnet using nine planes of a double-sided coordinate silicon detector. The particle speed ($\beta = v/c$) is measured by the TOF system, a transition radiation detector (TRD), and the RICH detector. The electromagnetic energy of particles is measured by the calorimeter (ECAL).

3. Test flight of AMS-01 on the space shuttle Discovery

The detector apparatus and especially its electronic components were designed on the basis of the electronics for accelerator experiments, which had not been used before in space installations. It was therefore necessary to make sure that the AMS would function in space conditions: vacuum, temperature changes from $-65\,^{\circ}\mathrm{C}$ to $40\,^{\circ}\mathrm{C}$, and intense radiation, which can damage electronic components. It was decided to perform a test flight on a space shuttle [7]. The detector had to withstand very strong vibrations (150 db) and high acceleration (3 g) at launch and deceleration (6.5 g) at landing. The test flight was performed in June 1998.

The detector operated in an almost circular orbit at a hight of 400 km and an inclination of the orbit plane of 51.8°, the ordinary orbit of the space station MIR that was then operational.

Figure 2 shows a schematic of the AMS-01 detector.

A permanent magnet was used as the analyzing element of the spectrometer. The magnet was constructed with a modern magnetic material, $Nd_2Fe_{14}B$. This made it possible to obtain a magnetic induction of 1.5 G in a sufficiently large volume. The magnet is of cylindrical shape, 80 cm in length and 116 cm in diameter. The magnetic field was close to uniform and directed orthogonally to the cylinder axis, ensuring efficient deflection of particles moving along the cylinder.

In Fig. 3, the magnetic field directions for the 64 sectors are given. The magnet was made of 64 sectors of the NdFeB material, each consisting of 100 $5 \times 5 \times 2.5$ cm^3 blocks; the highest-grade material with an energy level $(\mathrm{BH})_{\max} = 50$ MG Oe was used.

A magnet model at 1:3 scale was constructed to verify the magnetic field values obtained in the chosen configuration, and the values of the field, the magnetic moment, and the flux leakage were confirmed. Another model, now at full scale, was constructed to perform vibration and acceleration tests. And finally, a third model, also full scale, was built. It was

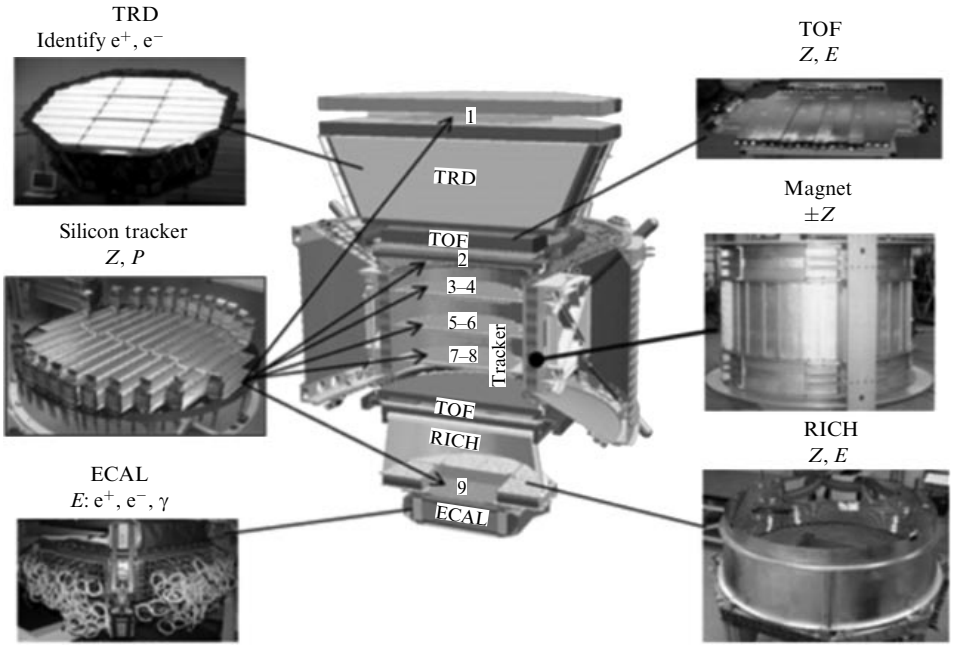

Figure 1. Configuration of the AMS detector on the ISS.

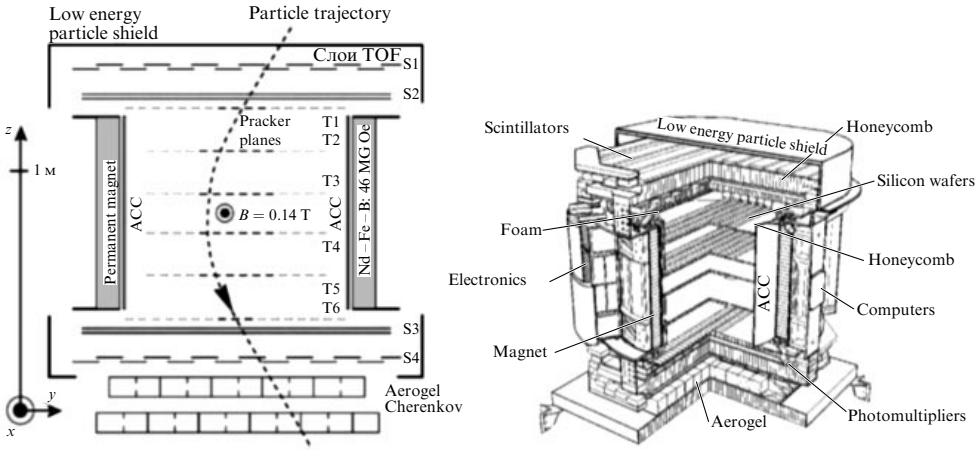

Figure 2. AMS-01 detector arrangement.

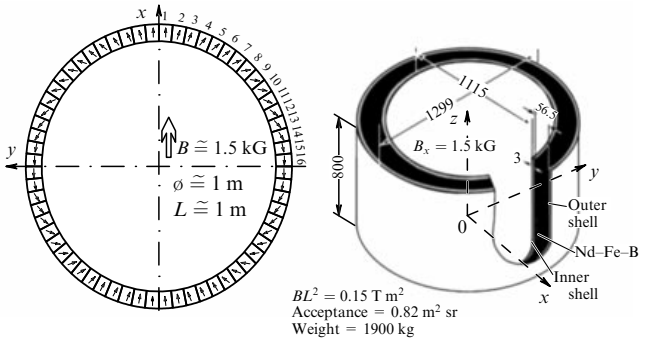

Figure 3. Permanent magnet arrangement. The magnetic field directions are shown.

constructed without using glue, according to NASA safety regulations, because the glue features were not known well enough, especially for using it in space conditions.

The NASA safety requirements for the magnetic field were as follows:

(1) The dipole magnetic moment had to be very small. A nonnegligible magnetic moment interacting with Earth's magnetic field would give rise to uncontrollable turning and twisting forces acting on the shuttle or space station. Because there was no past experience, NASA had doubts as to whether it was possible to construct a powerful magnet with a small enough dipole magnetic moment.

(2) To ensure the safety of space station personnel, the magnetic field leakage at a distance of 2 m from the magnet was required to be less than 300 G.

The actual magnet was very satisfactory as far as these requirements were concerned: the dipole magnetic moment was negligible and the leakage field was less than 3 G.

The measurement of the track curvature and thus determination of the momentum value and the sign of the particle charge was done by six layers of silicon coordinate detectors [8]. These detectors provided a micron accuracy of coordinate measurement, and at the same time the charge magnitude was measured by ionization loss. At the setup entrance and exit, the particle crosses scintillation counters of the TOF system [9]. Particle velocity was determined by measuring the time of flight on a base of 1 m, 150 ps being the typical accuracy of time measurement. By combining the momentum and velocity, the particle mass was determined. When the particle velocity was too high for the time-of-flight technique, the Cherenkov counter with an aerogel radiator (refractive index 1.035) was used for particle identification. The general detector arrangement is shown in Fig. 2, where the internal magnet surface is seen covered with an anti-coincidence counter [10], serving as a shield against particles interacting in the magnet material. A thin shield on top and another at the side eliminated the influence of Earth's radiation belts (low-energy electrons).

The detector had no cover and worked in the vacuum of space. All detector elements underwent careful testing during production and assembly to show that the space conditions of very high vacuum and large temperature variations did not worsen the spectrometer performance. Successful tests on vibration ensured the construction stability in intensive vibrations during the time when the space shuttle engines were on.

During the 10-days flight, about a hundred million events of cosmic-ray particles passing through the apparatus were detected. However, the shuttle was docked to the space station MIR during a considerable part of this period. At this time, the detector orientation was inconvenient for the AMS, for example, the detector was oriented toward Earth. In addition, the AMS field of view included some parts of the space station, and cosmic-ray interactions in its material produced an additional unwanted background. The useful exposure time when the AMS field of view included only open space was only 4–5 days.

The detector was provided with many temperature and magnetic-field sensors, and the continuous monitoring of the sensors during the flight helped determine the optimal temperature regime. The heaters that were also provided were not used, however, because the temperature turned out to be high (sometimes too high), and the temperature regime was adjusted by changing the orientation of the shuttle relative to the Sun. Online software monitored the performance of all detector systems.

The test flight revealed particularities of high-energy physics experiment in space flight conditions. The construction of the AMS detector gained a great deal when a practical understanding of technological possibilities and real characteristics of each detector component in space flight conditions was achieved. Two hours after launch on June 2,

1998, the detector was tested before putting it to work. In flight, the detector sat in the cargo bay of the shuttle and functioned in a vacuum. The trigger was produced by a coincidence of four TOF counter signals, which ensured the passing of a particle through the tracker. The detector performance, as well as the magnetic field and temperature, were continuously monitored. About a hundred million triggers were registered.

After landing, the detector underwent a series of detailed tests. It was put in a heavy-ion beam of the Darmstadt accelerator with the energy from 1 to 5.6 GeV and 600 different incident angles. The correct mass lines were obtained with the overall statistics of 45 mln events. Then the AMS was put in a proton beam with the energy ranging from 2 to 14 GeV and 1200 different incident angles. The statistics gathered comprised 100 mln events.

Continuous monitoring showed that the AMS characteristics before, during, and after the flight did not change.

In spite of the technical character of the AMS-01 flight, a large scientific program was implemented.

1. *Search for anti-helium in cosmic rays* [11]. For the 2.86×10^6 He nuclei observed by the AMS, not a single anti-He in the energy range up to 140 GeV was detected. If we assume that the spectrum shape for He and anti-He is the same, then the upper bound on the anti-He flux with respect to He flux would be 1.1×10^{-6} [12]. This is a considerable improvement compared to earlier measurements.

2. *Protons in near-Earth orbits*. Besides the primary spectrum of protons arriving on Earth from outside, the so-called second spectrum (albedo) was observed [13, 14]. The second spectrum is clearly observed at energies and at latitudes where primary protons cannot appear, that is, below the geomagnetic cutoff. The second spectrum trajectory reconstruction showed that all these protons are produced inside the atmosphere, and 70% of them come from a very narrow geographical region.

3. *Leptons in near-Earth orbits*. The electron spectra at 0.2–40 GeV and positron spectra at 0.2–3 GeV were measured. Two types of spectra were observed: the primary one at high energies and the second spectrum (albedo) at lower energies; in contrast to the primary spectrum, the number of positrons in the second spectrum substantially exceeds the number of electrons [15, 16]. As in the case protons, the fixes of the second-spectrum particles directed toward Earth and away from it are the same, which suggests their atmospheric origin. Reconstructions of second-spectrum trajectories shows that most of these leptons travel in Earth's magnetic field for a long time and originate from two symmetric geographical regions in the atmosphere, with the areas where electrons originate being sinks for positrons, and vice versa.

The ratio of the number of positrons to all leptons in the energy range of 1–30 GeV was measured.

4. *Helium in near-Earth orbits*. The helium spectrum at energies 0.1–100 GeV/nucleon was studied [17]. Above the geomagnetic cutoff, the spectrum follows a power law; below the cutoff, the second spectrum is observed and unexpectedly more than 90% of the spectrum corresponds to ^{3}He.

5. *Cosmic protons*. The AMS measured the primary spectrum in the range 0.2–200 GeV with a high accuracy [18], which is needed for the evaluation of atmospheric neutrino fluxes.

6. *Deuterons in near-Earth orbits*. About 10,000 deuterium nuclei at energies of 0.1–1 GeV/nucleon were observed [6].

7. *Search for anti-deuterium in cosmic rays*. For the measured deuterium flux of 1×10^4, no anti-deuterium nuclei were observed.

8. *Studies of trapped and quasi-trapped particles in near-Earth orbits*. An analysis of particle trajectories detected below the geomagnetic cutoff showed that trapped protons, electrons, and positrons exist and move along trajectories crossing the Brazilian anomaly [13, 14].

4. Main mission: AMS-02 on the International Space Station

4.1 Superconducting magnet

The design features of the AMS had to allow reaching the anti-helium/helium ratio levels better than $1/10^{10}$ and $e/p < 1/10^6$ for suppression of the proton background in a positron sample. The energy spectrum accuracy was to be better than 1%. The AMS energy range had to extend to several TeV [5].

These levels had to be achieved in any configuration of the AMS, whether the magnet was permanent or superconducting [19]. The superconducting magnet development was unique: it had to function autonomously in space conditions for 2 to 3 years. The magnet development took a considerable part of the time and resources.

Moreover, because it was not known which magnet — permanent from AMS-1 or superconductive — would finally be used, total magnet interchangeability had to be ensured. The field shape was identical (Fig. 4), with all geometrical parameters allowing the same detector elements to be mounted with any magnet.

The superconducting magnetic system of AMS-2 (see Fig. 4) consisted of two large dipole coils, a Helmholtz pair generating most of the field, and 12 smaller flux return coils that served to control the stray field and the dipole moment also contributing to the dipole field. The coils were situated inside a vacuum volume and worked at the temperature of 1.8 K. They were mounted outside the helium volume and provided with a nontrivial refrigeration system; in the unlikely event of quenching, it allowed cooling the coils using the available liquid helium.

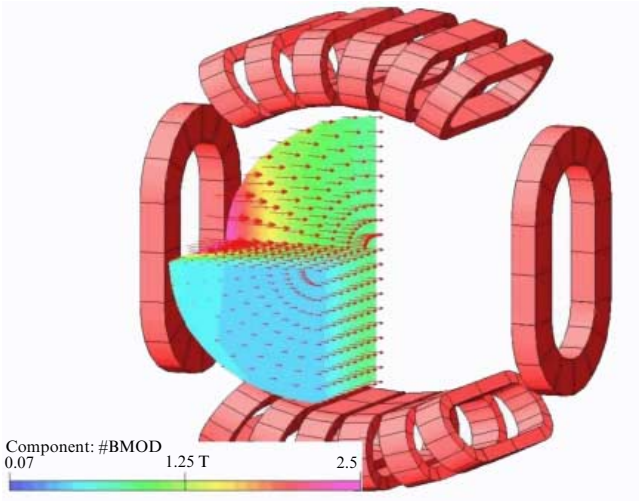

Figure 4. Superconducting magnet coil arrangement that allows achieving a field configuration identical to that of a permanent magnet; in both cases, the inner radius was the same, the dipole moment was negligible, and the stray field 2 m from the center was less than 300 G.

The coils were made of a new aluminum-stabilized conductor of a small cross section, which was developed especially for the AMS by the ETH Zurich group. The conductor reduced the probability of quenching by a factor of 2000. This new material is produced in Zurich in considerable quantities and is now widely used in high-energy physics experiments.

The AMS magnetic system consisted of superconductive coils, the superfluid helium volume (2500 l), and a cryogenic system, all situated in a vacuum enclosure; the electronics, valves, and cable systems were outside the enclosure. At the moment it was switched on, the magnet was cooled to the working temperature (1.8 K) with no current. The current was put on after installing the AMS on the ISS. After the beginning of work, the helium was not replenished and gradually evaporated. In 2 to 3 years, all the helium evaporates, which determines the functional lifetime of the AMS.

The produced coils are shown in Fig. 5. During production, the magnet underwent a number of tests. Figure 6 demonstrates magnet transition to the stable temperature regime, the stability condition being $dT/dt < 0.0001$ K hr^{-1}.

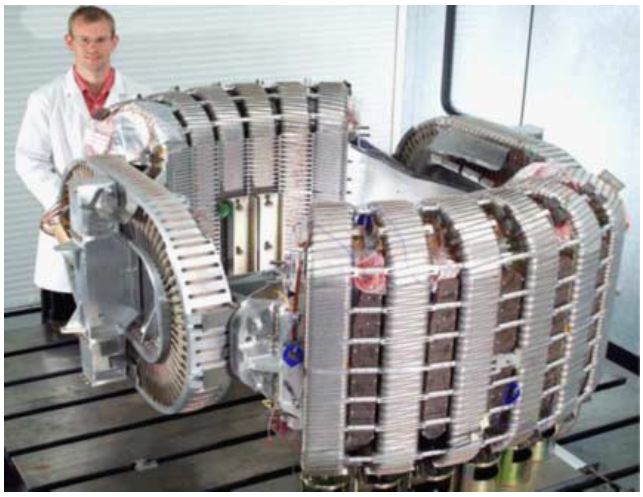

Figure 5. Assembly of the manufactured magnet coils.

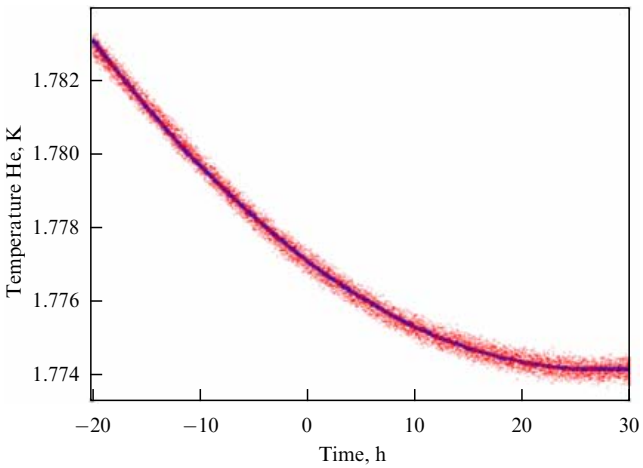

Figure 6. Stabilization of the AMS helium volume. The stability condition is $dT/dt < 0.0001$ K h^{-1}. The expected lifetime of the AMS cryostat is 28 ± 6 months.

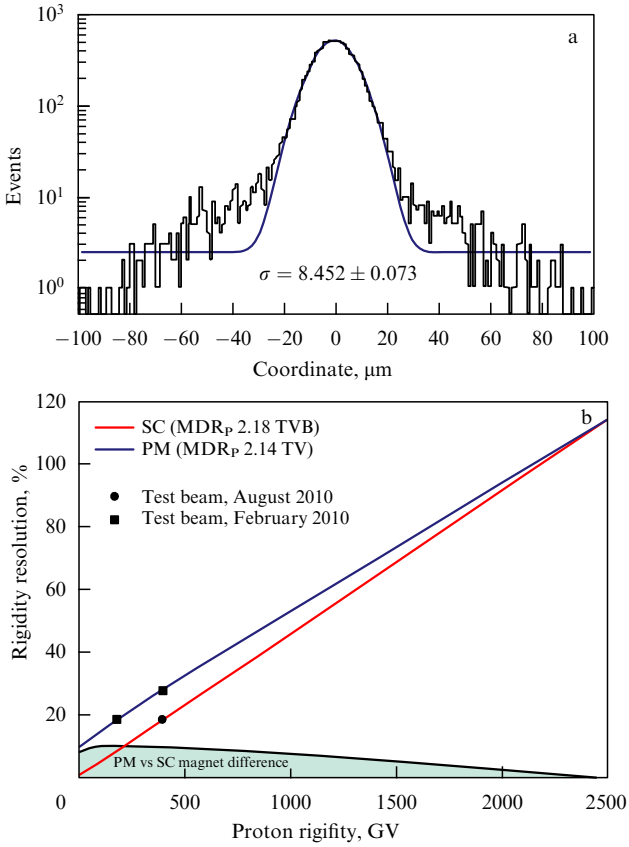

Figure 7. (Color online.) (a) Coordinate resolution measured for a tracker plane in a 120 Gev muon beam the width is 8.5 μm. (b) A comparison of momentum resolutions: the red line for superconductive and the blue line for permanent magnets.

Tests of the fully assembled AMS setup were conducted using CERN accelerator beams in 2010.

The superconductive magnet was then removed and a permanent magnet was mounted in its place. The results of measurements of the coordinate resolution are given in Fig. 7a, and in Fig. 7b the momentum resolutions are compared: the red line corresponds to the superconductive magnet and the blue one to the permanent magnet.

4.2 AMS-02 composition

The AMS detector was constructed according to the design, i.e., with a superconductive magnet, which was to originally work for 2 or 3 years, in accordance with the expected lifetime of the ISS. However, in 2010, NASA announced that it had decided to extend the functioning of the ISS to 2020 and maybe even to 2028.

To use the increased lifetime of the ISS, taking into account that replenishing the He reservoir in orbit is impossible, the superconducting magnet had to be replaced with a permanent one.

The magnetic field of the permanent magnet has not changed within the initial measurement accuracy (1%) over the 12-year period.

We discuss at the main AMS components.

The AMS coordinate detector (*tracker*) is currently the biggest (6.7 m^2) tracking detector built for space research [20]. The accuracies achieved are quite high even for ground-based trackers. The AMS-01 test flight proved the successful adaptation of accelerator technologies to space conditions

and the technological feasibility of producing large-surface coordinate detectors. The semiconductor detecting elements of the tracker were made of thin silicon wafers with longitudinal strips on one side and orthogonal strips on the other. It has become possible to measure the $x-y$ coordinate with one detector, thus ensuring a minimum amount of material (0.3% of the radiation length) as the particle passes. The readout pitch was 27.5 microns in the projection measuring curvature, and 300 microns in the other. Over 4000 sensors were produced to select the 2500 units of the highest quality for the tracker.

The quality of the tracker was verified in a series of tests, including tests of the tracker elements, and then studies in the minimum ionizing particle beams and in light and heavy-ion beams were made. The result of the measurements of the coordinate resolution in a 120 GeV muon beam, given in Fig. 7 as an example, was the width of 8.5 microns in measuring the momentum projection and 30 microns in the other projection.

Transition radiation detector. Transition (X-ray) radiation arises when a particle passes an interface of two media with different electric characteristics; the interface transforms the field of the particle charge. The radiation intensity is proportional to the particle gamma factor, and this makes it possible to separate particles, because the gamma factor of electrons with the energy of a few GeV is greater than that of protons of the same energy by three orders of magnitude. Transition radiation (TR) was detected in layers of straw tubes interspersed with 2 mm thick fleece [21]. The straws were filled with an $Xe-Co_2$ gas mixture, the best detection range being $500 < \gamma < 10000$. Figure 8a illustrates the result of a test of a single TR layer. The TR contribution is very clearly seen. Figure 8b shows how efficiently the TR suppresses the proton background while detecting 90% of the electrons.

Time-of-flight counters [9] provided a fast trigger selection of particles entering the solid angle of the setup, measuring the time of flight, including separation of particles coming from above and from below, and performing the particle charge measurement. The TOF system was developed on the basis of the well-known scintillation technique, which allowed reaching a time resolution of 160 ps. The TOF system and, accordingly, the entire AMS setup have a geometrical acceptance of 0.4 m^2 sr. The TOF comprised four planes of scintillation counters: two planes situated above the magnet and two below; the sensitive area of the plane was 1.2 m^2, and the plane was made with an overlap of scintillators to avoid cracks. The two top planes had scintillators directed orthogonally, and the same was done for the two bottom planes. Ionization losses were measured by the TOF system with a resolution sufficient to determine the charge up to $Z > 26$. The measurement range which was needed and ensured was 10,000. The features achieved were mechanical stability, radiation resistance, and stability in the temperature range $-20-+50\,^{\circ}C$; double redundant electronics guaranteed the system operation for many years on board the ISS.

Figure 9 illustrates the AMS potential by showing the measurement data for the spectrum of cosmic-ray nuclei. The results of ionization measurements by TOF and the tracker are given.

Anticoincidence counters [10] were situated on the inner surface of the magnet surrounding the tracker, thus protecting it from the particles penetrating through the side surfaces of the magnet. The neighboring counters were joined by dovetail for hermeticity.

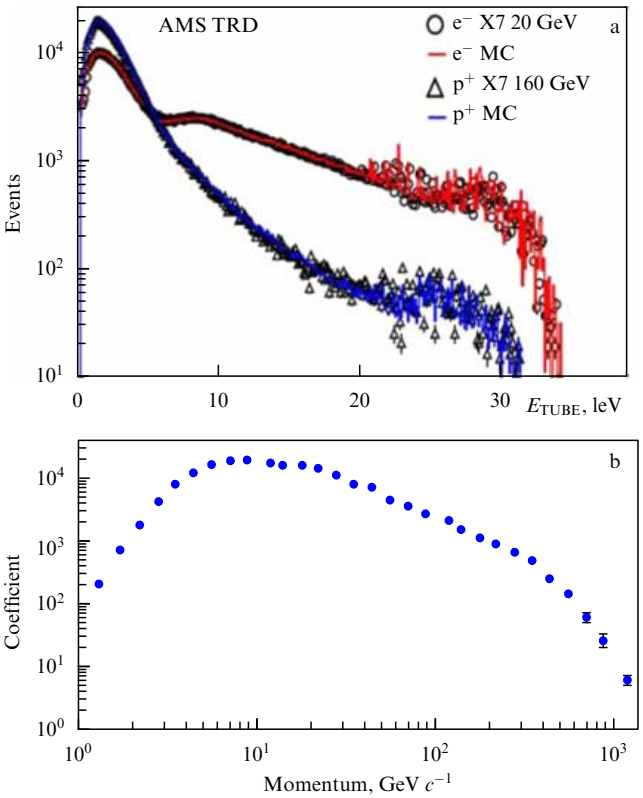

Figure 8. (a) Beam test of a single TRD layer. (b) Energy dependence of the proton suppression coefficient when the electron detection efficiency is 90%.

RICH detector [22]. Many tasks of the AMS physics program needed precision measurement of the particle mass. The particle momentum is measured by the AMS magnetic spectrometer, but to measure the velocity precisely, a special Cherenkov detector, RICH, ensuring the relative accuracy of 1/1000, was developed. RICH has a large geometrical acceptance and works in a vacuum and the low temperature of open space. Photons are radiated into a cone with the opening angle 2θ, $\cos\theta = 1/\beta n(\omega)$, and the threshold velocity $\beta_{min} = 1/n(\omega)$, where $n(\omega)$ is the radiator refractive index. The number of photons emitted in the frequency range $d\omega$ after the particle passes a distance dx is $d^2N/d\omega\, dx = \alpha Z^2 \sin^2\theta$; thus, the opening angle is defined by the particle velocity and the number of photons emitted by its charge (Ze).

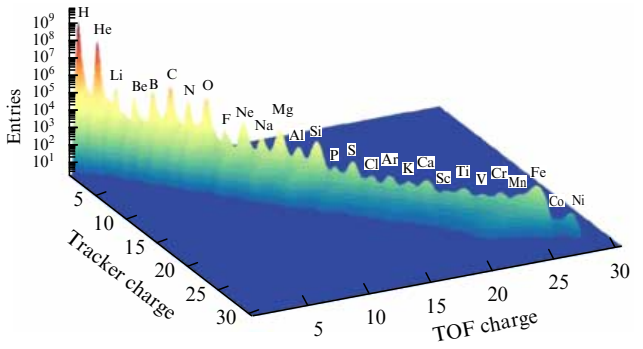

Figure 9. Measured spectrum of cosmic-ray nuclei by the ionization measurement of the TOF system and the tracker. This is an illustration of the AMS features.

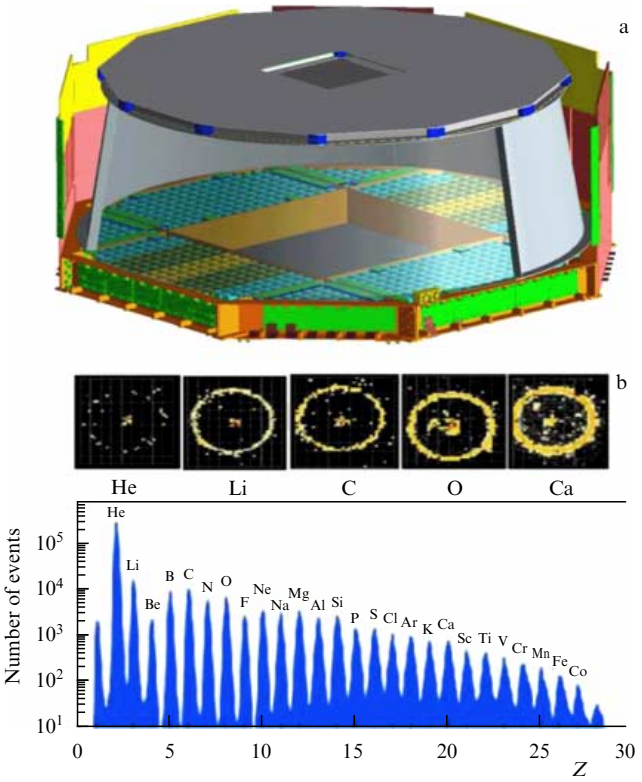

Figure 10. (a) The RICH structure. (b) Snapshots of the rings of Cherenkov radiation for different nuclei. In the bottom part: the charge spectrum of nuclei taken in a heavy-ion beam.

The RICH structure is shown in Fig. 10a. The radiator is on top and consists of two parts: the peripheral one is made of silica gel having the refractive index 1.05, and the central part (Fig. 10a), where the NaF radiator is situated, with the refractive index 1.336 to cover smaller energies. Cherenkov light is reflected by the side reflector and detected by phototubes sitting at the bottom of RICH. The result is illustrated in Fig. 10b, where snapshots of the Cherenkov rings for different nuclei are shown. The radii of the rings determine the particle velocity, and the signal magnitude determines its charge. At the bottom part of Fig. 10b, the charge spectrum obtained in a heavy-ion beam is shown.

The total absorption counter — electromagnetic calorimeter (*ECAL*) — very precisely measures the energy of electrons and positrons and efficiently separates them from hadrons. The hadron suppression is 10^4 for the energy range 1.5 GeV to 1 TeV. The calorimeter is made of a multilayer assembly of thin (1 mm) lead plates interspersed with layers of scintillating fibers (1 mm), the total thickness of the calorimeter being 16.7 rad. len. [23]. The calorimeter is composed of blocks, each containing 11 lead layers interspersed with 10 fiber layers; the fibers in a block are oriented in the same direction, but the blocks are mounted in the calorimeter so as to alternate x and y orientations of fibers. In this way, a three-dimensional reconstruction of events is achieved. As shown in Fig. 11, the energy resolution is 2–3%, the angular resolution is 1°, and suppression e/p $\sim 10^4$ up to energies of 200 GeV and above.[1]

[1] Such an e/p suppression was achieved by using: (1) the BDT (Boosted Decision Tree) classification method [24] with 12 parameters of event measurement, (2) detailed Monte Carlo event simulation at energies up to 1 TeV and calibration in high-energy beams up to 400 GeV of CERN SPS, (3) identification of electrons and positrons in TRD. For details, see [25].

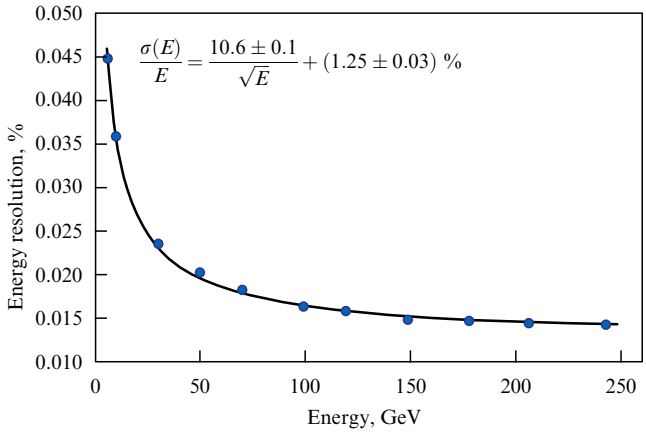

Figure 11. Energy resolution of the calaorimeter as a function of energy; data obtained in a high-energy electron beam.

The AMS electronics [6] is based on the latest high-technology developments used in experimental particle physics and adapted for orbit conditions. NASA provided the electrical connection of the AMS to the ISS systems to power the AMS via low-rate (LRDL) and high-rate (HRDL) links.

ISS electric power was provided by eight large solar panels. The AMS had two lines, each fed from one panel; the maximum power authorized for the AMS was 2400 W. The AMS satisfies nontrivial NASA requirements on electrical insulation, groundings, electromagnetic interference, current drops, and impedance.

Telemetric data, the monitoring of which provided complete control of all AMS elements, were transferred through the LRDL, and if needed the LRDL was also used to transmit commands coming from Earth, to change the working AMS parameters. The maximum information volume authorized for the AMS and transferred through the LRDL was 20 kbit s^{-1}. The bulk of AMS data was transmitted through the HRDL. The AMS data entered the ISS with a speed up to 60 Mbit s^{-1}. Then, with the help of auxiliary satellites (TDRS), the transmission to Earth in the radio (KU) range was done with a speed up to 43 Mbit s^{-1}. The AMS orbit average range was up to 10 Mbit s^{-1}. The AMS used an intermediate buffer on one of the four computers of the readout system.

The information flow was determined by the trigger system, i.e., by coincidence of the TOF signals with no signals in the anticoincidence system. The rate varied from 200 to 2000 Hz. The AMS electronics were designed to work at twice that rate.

A dedicated computer, an AMS laptop, served as a data archive and an additional command module under crew control. The full AMS electronics contained 300,000 channels, equivalent to the rest of the ISS electronics.

The long duration of the AMS mission demanded a new approach to the organization of the ground-based data analysis complex for the data continuously arriving from the ISS. A system consisting of two units was organized at CERN.

• The Payload Operations and Control Center (POCC) served for control, selective sample analysis, and operations. A group of physicists worked there around the clock seven days a week and controlled all AMS systems and, with the help of commands sent to the ISS, corrected the performance

of the AMS elements. AMS control and command are done exclusively from the POCC.

• The Science Operations Center (SOC) is the center for mass physical reconstruction and analysis of the data. The existing software allows analyzing data at the same rate as the data are collected.

AMS temperature control [26] is one of the most complicated tasks and demands constant attention. Continuous observation of the temperature variation of the detector elements is the main task of the group of physicists constantly present at the POCC. The thermal environment in space surrounding the AMS is very complex. Depending on the ISS position, different parts of the detector undergo a fast change in direct solar irradiation, followed by the deep cold of outer space. The AMS itself emits 2 kW of power. Albedo (thermal radiation from Earth) should also be taken into account. In such conditions, because the functioning of different detectors depends on temperature, the temperature of the detectors should not only be within some range but also be stable in time. Solar radiation plays a major role in the AMS thermal conditions, the amount of solar radiation being determined by the angle β between the ISS orbit plane and the direction to the Sun; this angle changes from -75.1° to 75.1° , and if β is more than 70°, the whole orbit is exposed to the Sun, and if β is near zero, about 40% of the orbit is in Earth's shadow. Most of the time β is in the range between -50° and $+50^\circ$.

In view of the complex thermal conditions of the AMS, a very detailed computer model has been developed that takes all sources of heat into account: external, such as solar radiation, and internal, such as 2000 W from the AMS electronics. To radiate the heat fluxes outside the AMS, panel radiators are used, and their geometrical positions were carefully modeled because different parts of the detector are irradiated and radiate differently. This task required many iterations and studies of many variations. Figure 12 shows the final configuration of the AMS radiators; the values of power radiated into open space are also given.

The final model verification took place at the center of the European Space Agency in the Netherlands. The AMS detector was put in a large thermo-vacuum chamber normally used for satellite testing. The space flight conditions (the vacuum, temperature, solar radiation, etc.) were exactly reproduced in the chamber. The AMS worked in such conditions with corresponding variations of temperature and other parameters. The test confirmed the conclusions of the thermo-model used.

The continuous thermal control of the AMS was one of the most difficult tasks for the personnel, because such problems had not existed in the past accelerator experience of the physicists.

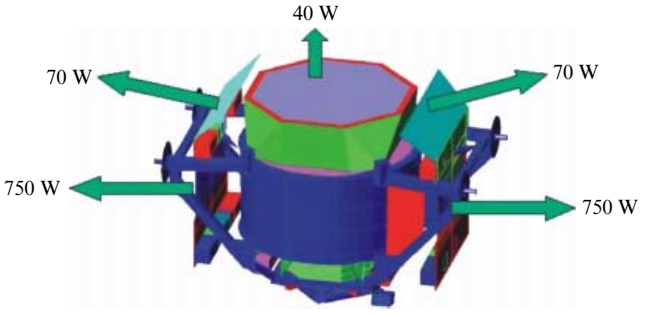

Figure 12. Configuration of the AMS radiators; the values of power radiated into open space are also given.

5. Physics results and their interpretation

The results obtained by the AMS in 2011–2015 were published in [27–33].

By the generally accepted theory, cosmic rays propagate through the Galaxy by diffusion; scattering on the inhomogeneities of a magnetic field and interstellar radiation gives rise to energy losses. Nuclei undergo the processes of collisions and radioactive decay leading to fragmentation. Cosmic-ray spectra are also modified by convection caused by the galactic wind and interstellar shockwaves, where particle acceleration takes place. The cosmic-ray spectrum on Earth is therefore considerably different from the one emitted by the source. Secondary electrons and positrons arise by collisions of protons with protons and nuclei of the interstellar medium. The pions and kaons also produced in collisions finally decay into leptons. The GALPROP computer program [34] is widely used at present to describe the propagation of cosmic rays and is the most developed. Its results serve as the basis for the modern 'standard' description of the origin, acceleration, and propagation of cosmic rays. However, GALPROP relies on a number of essential approximations: cosmic rays originate from the remnants of supernova explosions with a continuous distribution of sources, and the propagation of cosmic rays is isotropic.

Most of cosmic-ray electrons are assumed to be 'primary', i.e., produced and accelerated in the remnants of supernova explosions. But positrons are 'secondary', produced in collisions of hadrons with nuclei of the interstellar medium. In this concept, the spectra of electrons and positrons have no features at TeV energies, and the positron-to-electron ratio should monotonically decrease.

The source of the observed electrons and positrons is estimated to be located not farther than 1 kps away, and therefore the spatial distribution and the emission spectrum in a given area can be substantially different from predictions based on the isotropic distribution of averaged sources.

The 'standard' picture leads to the generally accepted description of the spectrum by a power-law function,

$$\Phi = CE^{\gamma} ,$$

with a constant index γ in the energy range from 10 GeV to 100 TeV. This is natural if we assume that the proton acceleration occurs in supernova explosions, which spread over the Galaxy disk uniformly. The index is close to three and is chosen according to measurements for different particles.

Lepton spectra had been measured several times before the AMS. Recent measurements at energies in the TeV range were taken in the experiments ATIC [35], HESS [36], MAGIC [37], FERMI [38], and PAMELA [39]. Comparing the results, we see that one of the main difficulties is a systematic disagreement of the data from different detectors. The PAMELA data approach the correct accuracy level, but only the AMS-02 precision measurements settle the problem.

5.1 Electrons and positrons

5.1.1 Spectrum analysis. The AMS precision measurements of electron and positron spectra were based on a total sample of 4.1×10^{10} events in the energy range 0.5–700 GeV for

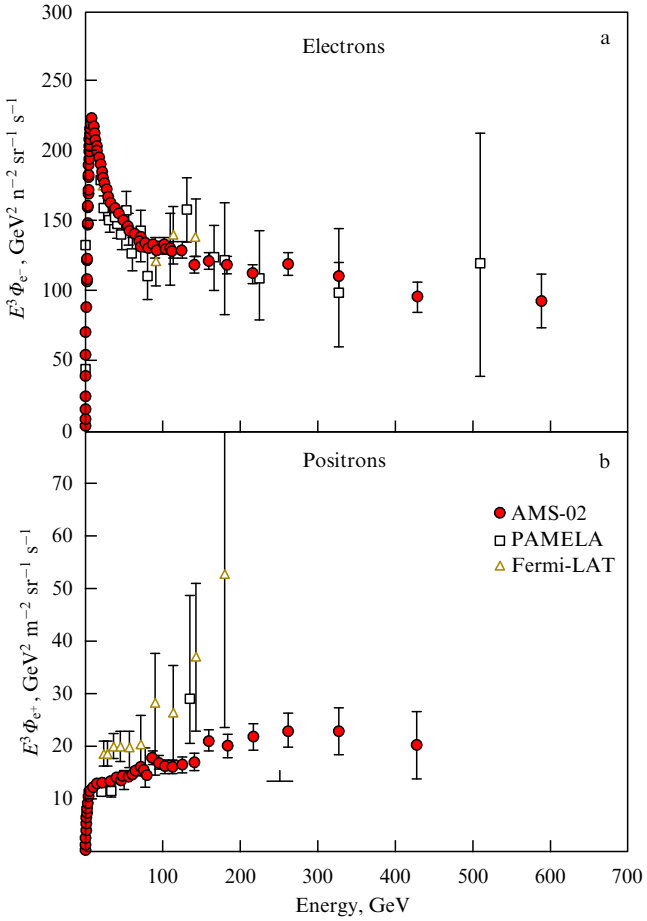

Figure 13. AMS results [30]. (a) Electron and (b) positron spectra multiplied by E^3; also shown are data from [38, 39].

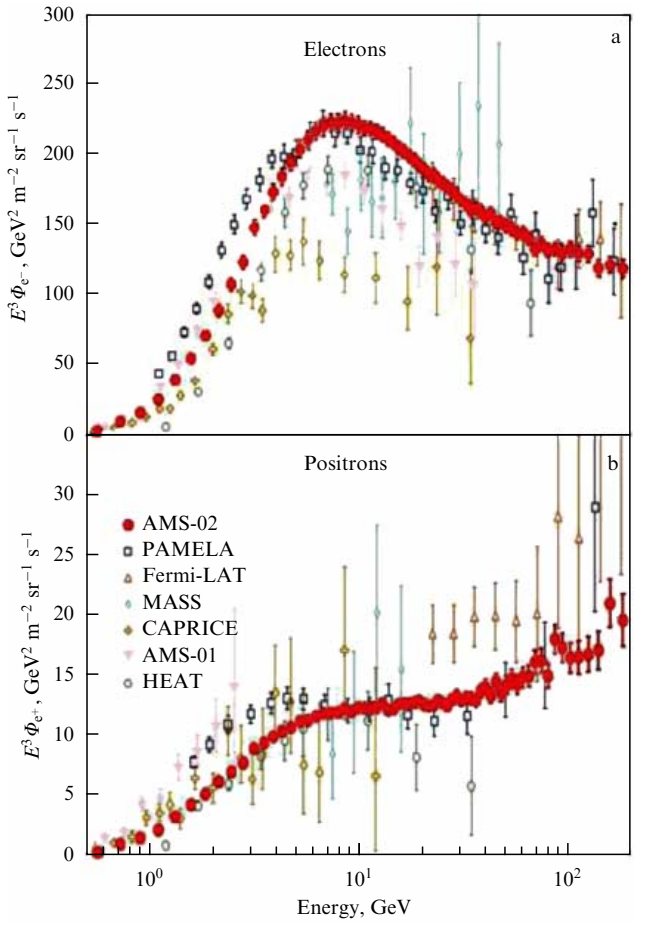

Figure14. AMS results [30]. (a) Electron and (b) positron spectra multiplied by E^3 for energies below 200 GeV in comparison with the data in [16, 38–42, 44].

electrons and 0.5–500 GeV for positrons. The AMS spectrum measurement results multiplied by E^3 are given together with recent measurements in Fig. 13. In Fig. 14, spectra below 200 GeV are considered in more detail. At energies below 10 GeV, both electrons and positrons are influenced by the solar modulation; this is noticeable in the flux change when the measurements lasted long enough. For energies above 20 GeV, the influence of solar modulation is insignificant. In the range 20–200 GeV, the electron spectrum decreases faster than the positron spectrum, i.e., the electron spectrum is softer. This may mean that either the positrons are primary or the electrons are secondary, or maybe both, and in any case this is difficult to explain in the framework of the traditional model of diffuse propagation of cosmic rays.

As can be seen in Fig. 13, neither the electron nor the positron spectrum can be approximated by a power law with the same index in the whole energy range studied.

For the detailed analysis, the energy spectra were fitted using a sliding window with the width sufficient for reliable determination of the local γ value:

$$\Phi_{e^\pm}(E) = C_{e^\pm} E^{\gamma_{e^\pm}}, \ \gamma_{e^\pm} = \frac{d[\log \Phi_{e^\pm}]}{d[\log E]}. \quad (1)$$

The result is given in Fig. 15. A lower bound on the energy above which the spectrum can be approximated by a power law with index is 27.2 GeV for positrons and 52.3 GeV for electrons.

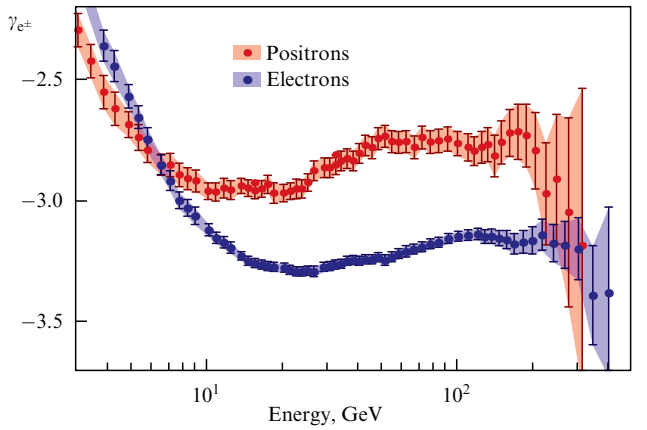

Figure 15. Spectral indices γ_{e^-} and γ_{e^+} as functions of energy. The 68% confidence limits are also shown.

Above 20 GeV, i.e., beyond the solar modulation influence, the spectral indices are different: γ_{e^+} is much greater than γ_{e^-} in the energy range 20–200 GeV. This implies that the reason for the increase in the positron fraction with energy is that the positron spectrum becomes harder, rather than the electron spectrum becoming softer above 10 GeV.

The results of measurements of the summary spectrum of electrons and positrons [29] are shown in Fig. 16 along with earlier, less accurate measurements. Determination of

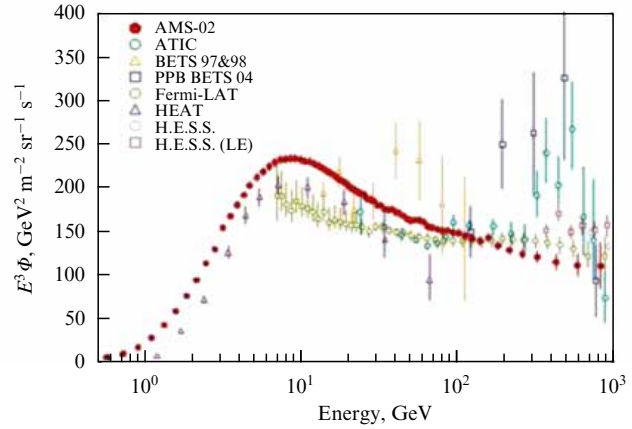

Figure 16. Summary electron + positron spectrum measurement together with earlier data [32, 36–39, 50].

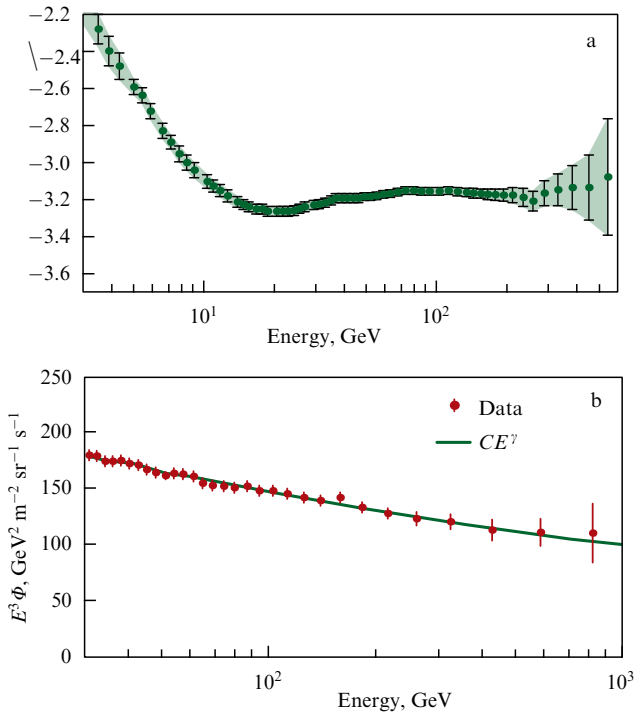

Figure 17. (a) Index of the summary spectrum. (b) Fit of the summary spectrum by a power-law function.

the energy dependence of the spectral index using (1) is seen in Fig. 17a. Multiplied by E^3, the spectrum $\Phi(e^+ + e^-)$ (see Fig. 17b) can be described above 30 GeV and up to 1 TeV by a single power-law function (1) with $\gamma = -3.170 \pm 0.008$.

The positron fraction $\Phi_{e^+}/(\Phi_{e^+} + \Phi_{e^-})$ was measured in the energy range 0.5–500 GeV. The results of AMS measurements of the positron fraction energy dependence in two energy intervals [28] are shown in Figs 18 and 19. Figure 18 shows that the positron fraction rapidly decreases in the energy range 1–8 GeV, as was predicted in the 'standard' picture of diffusion production of positrons as secondary particles. The decrease is then superseded by steady growth, which, as we see in Fig. 19, stops at about 200 GeV. The results of earlier experiments [16, 36, 38–43] are also given in Figs 18 and 19. The AMS data are much more accurate, making it possible to perform a quantitative analysis and comparison with models.

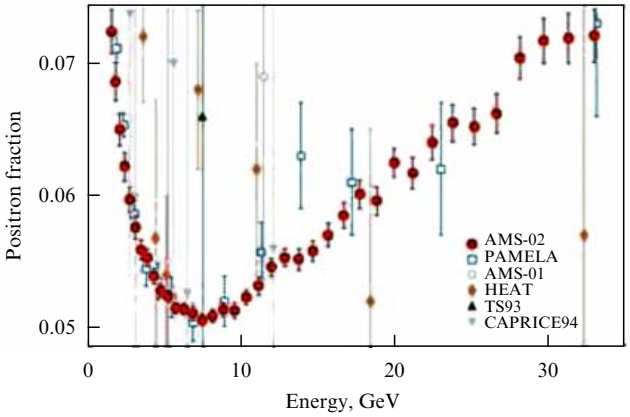

Figure 18. Energy dependence of the positron fraction at the energies 1–35 GeV. The data in [16, 39–42] are also shown.

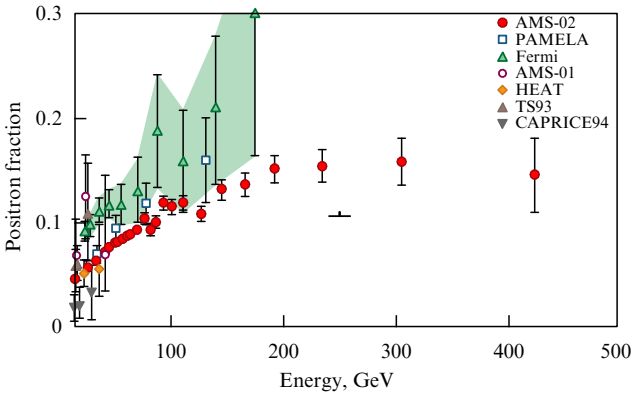

Figure 19. Energy dependence of the positron fraction at the energies 10–500 GeV. PAMELA [39], and FERMI-LAT [38] data, as well as others [16, 36, 40–42], are also shown.

The slope of the positron fraction energy dependence described by a linear function is shown in Fig. 20a,

$$S = c \log \frac{E}{E_0},$$

where c is a normalization factor and $E_0 = 275 \pm 32$ GeV is the energy at which the functions S crosses the abscissa axis, i.e. the energy at which the positron fraction attains a maximum.

The measurements of the positron fraction energy dependence are compared with the so-called 'minimal model', where the electron flux Φ_{e^-} and the positron flux Φ_{e^+} are described by the sum of a power-law function (diffusion term) and a term common to e^+ and e^- (source spectrum):

$$\Phi_{e^+} = C_{e^+} E^{-\gamma_{e^+}} + C_s E_s^{-\gamma} \exp\left(-\frac{E}{E_s}\right),$$

$$\Phi_{e^-} = C_{e^-} E^{-\gamma_{e^-}} + C_s E_s^{-\gamma} \exp\left(-\frac{E}{E_s}\right).$$

The coefficients C show the relative weight of the corresponding components, γ is the spectral index, and E_s is the source spectrum cutoff energy. Results of a fit with five parameters are shown in Fig. 20b. The parameter values are $C_{e^+}/C_{e^-} = 0.091 \pm 0.001$, i.e., the weight of the diffusion positron

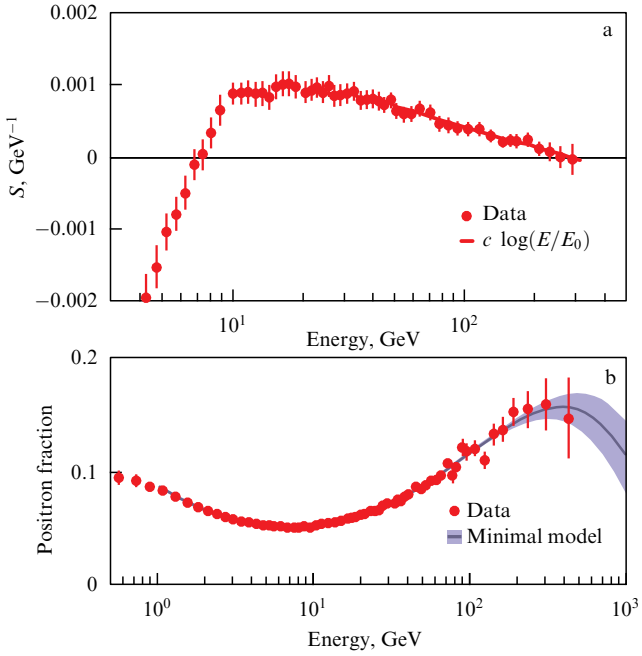

Figure 20. (a) Slope of the energy dependence of the positron fraction. (b) Comparison with the minimal model. The fit is done in the interval 1–500 Gev.

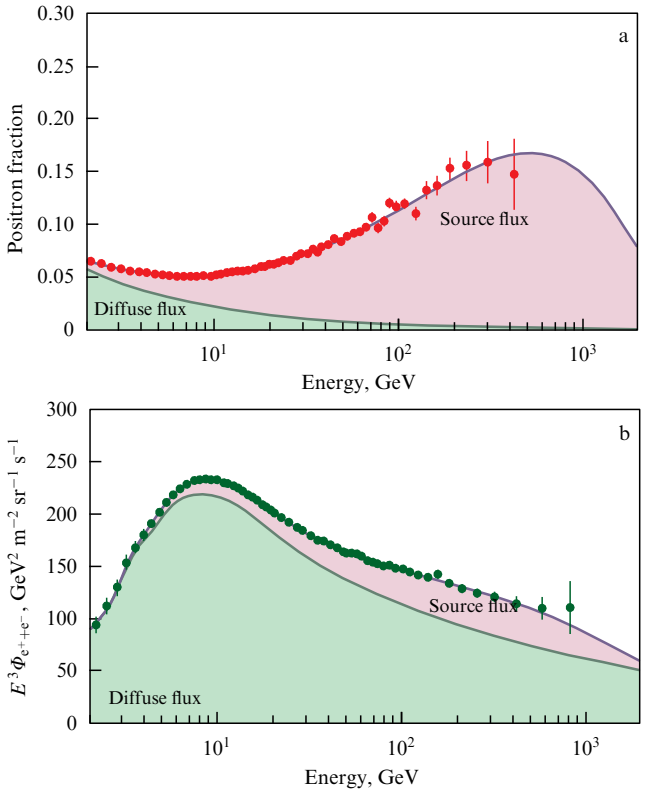

Figure 21. (Color online.) (a) Minimal model spectrum contributions to the positron fraction energy dependence. (b) The same for the summary electron + positron ($e^+ + e^-$) spectrum. The source spectrum is shown in pink, the diffusion spectrum in green.

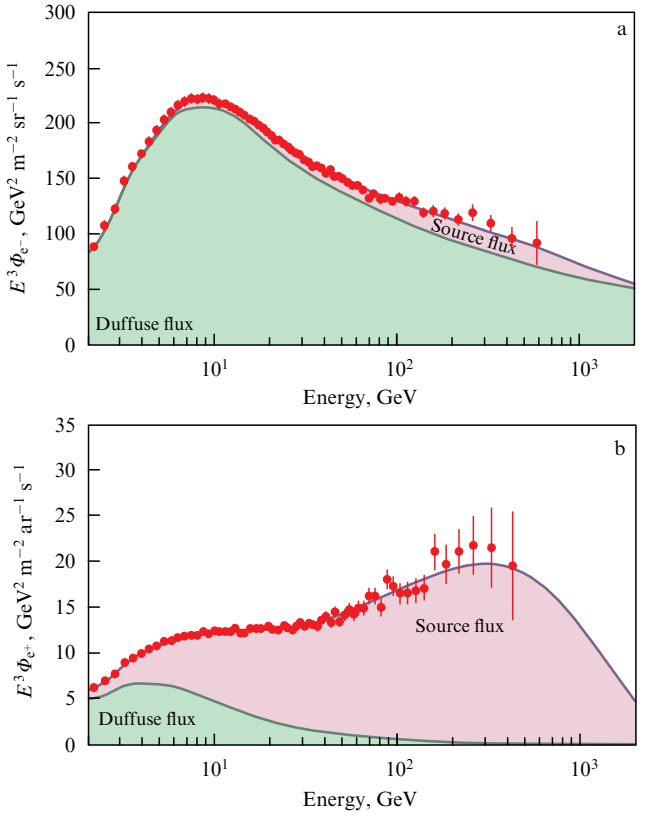

Figure 22. (Color online.) Minimal model spectrum contribution to the energy dependence of (a) electrons and (b) positrons.

spectrum is 9% of the corresponding electron spectrum. The parameter values $C_s/C_{e^-} = 0.0061 \pm 0.0009$ mean that the common source spectrum weight is 0.6% of the diffusion electron spectrum. A comparison of the spectral indices shows that the diffusion positron spectrum is softer than the corresponding electron spectrum, in other words, it decreases faster with energy, although the diffusion electron spectrum decreases faster with energy than the source spectrum does.

A more detailed comparison with the minimal model is illustrated in Figs 21 and 22, where the contributions of the diffusion spectra and the common source spectrum are shown. We can see in Fig. 21a that the leading contribution to the positron fraction, especially at high energies, is made by the source spectrum, while in the $e^+ + e^-$ spectrum (Fig. 21b), the character of contributions is totally different: the diffusion term dominates. The same picture is seen in the spectrum of electrons and positrons: again, the leading contribution to the positron spectrum comes from the source spectrum and to the electron spectrum, from the diffusion term.

We now discuss how the 'standard' ideas about the origin and propagation of electrons and positrons in cosmic rays agree with this picture. The cosmic-ray acceleration mechanism in expanding nonrelativistic shock waves arising from a supernova explosion predicts a power-law particle energy spectrum with a cutoff at high energies,

$$C\left(\frac{E}{E_0}\right)^{-\gamma} \exp\left(-\frac{E}{E_s}\right), \qquad (2)$$

which exactly corresponds to the 'source' spectrum in Figs 21 and 22. The spectral index γ usually turns out to be about 2, although with a large uncertainty. The diffusion term also has the energy dependence described by a power law, but without an exponential cutoff; hence, the chosen shape of the secondary electron and positron spectrum (see Figs 21 and 22) again corresponds to predictions of the 'standard'

schemes. If we consider the minimal model seriously, then it follows from Figs 21 and 22 that the positron spectrum is mainly the source spectrum, i.e., the positrons are primaries and most of the electrons are secondaries, entirely contradicting the expectations. The AMS data (see Figs 18 and 19) rule out an explanation of the positron fraction increase with energy by experimental errors or by statistical fluctuations. Immediately after the AMS result was made public, numerous publications explaining the phenomenon appeared. The number of such publications now exceeds several hundred. This large quantity alone means that a convincing explanation is still missing.

5.1.2 Standard picture. We briefly consider some physical assumptions that, in principle, allow quantitatively reproducing the positron excess.

1. In the standard approach, the acceleration of secondary positrons can be introduced in the same region where the primary electrons are accelerated. This can create an excess of high-energy positrons [47].

2. In [48], it is assumed the positron excess originates in a supernova explosion in a dense gas cloud, which happened recently and not far from us. Electrons and positrons are produced in hadron interactions inside the cloud, their spectrum being harder because the supernova spends more time in the radiative stage. Calculations performed in the framework of this idea show that with properly chosen parameters, the result can be in accordance with the AMS data.

3. A similar model is considered in [49]. The primary electrons, like other primaries, are accelerated only in the shock-wave plasma; secondary positrons are produced in hadron collisions in the source and can be accelerated in a region about the diffusion length in size. This leads to a harder spectrum, and consequently to a positron excess.

4. Other secondaries, not only positrons, can also be accelerated, and this can lead to an increase in the boron/carbon and antiproton/proton ratios. A detailed analysis shows that if more than 25% of high-energy positrons are secondaries accelerated in shock waves of the supernova remnants, they cannot be put into agreement with the observed B/C ratio. The antiproton/proton ratio is critical, however. Because a substantial increase in the $\bar{\mathrm{p}}/\mathrm{p}$ ratio with energy is not observed, this rules out, with high probability, any still existing possibility of the positron fraction increase coming from the acceleration of the secondaries in shock waves [50].

5. In the so-called nested leaky-box (NLB) model (incorporating regions with energy leakage) [51], particles are accelerated by a large number of sources scattered over the Galaxy. Each source is surrounded by a cocoon-like domain where interactions and spallation of nuclei take place, but without new acceleration.

The commonly accepted model of cosmic-ray propagation assumes a distribution of sources that is spatially smooth and constant in time, sending cosmic rays into interstellar space. It is assumed that the cosmic rays undergo diffusion in the Galaxy with a diffusion coefficient K that increases with energy $\sim E^{\alpha}$. Secondary nuclei produced in interactions of the primary nuclei with the medium also undergo diffusion with a similar diffusion coefficient. At the height of 500 parsecs, cosmic rays leak out of the Galaxy and are lost. The time of their stay in the Galaxy decreases with energy as $\tau \sim 1/K \sim E^{-\alpha}$, showing fast leakage of energetic particles

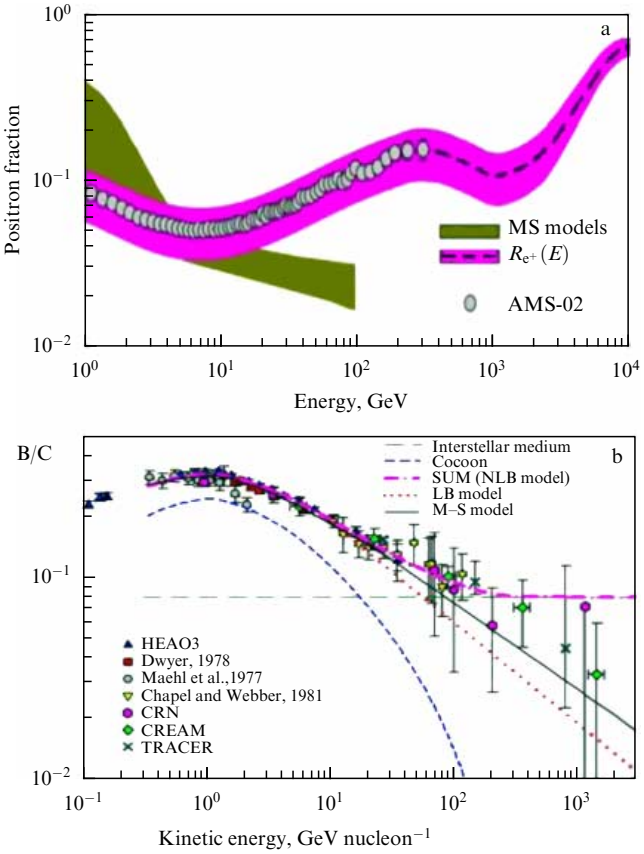

Figure 23. (Color online.) (a) Positron fraction energy dependence for the commonly accepted model (green) and its modified version (violet) [51] compared with the AMS-02 data. (b) The B/C ratio from [51].

from the Galaxy. The secondary particle spectrum decreases faster, and ratios like B/C turn out to decrease with energy. The strong correlation of positrons and boron nuclei at energies above 50 GeV is inevitable in these models. At energies above 50 GeV, such spectra are not in good agreement with observations. Modifying the existing model by taking into account that positrons contain only 3–5% of the parent proton energy while secondary nuclei (for example, boron) contain up to 100% of the energy per nucleon of the parent nuclei, and in addition taking the discrete, not uniform, distribution of the sources into account, it turns out to be possible to reconcile the model with measurements of the positron fraction in the entire measured energy interval (Fig. 23a). But the energy dependence of the decreasing B/C ratio describes the experiment much worse. From Fig. 23b, it can be seen that although the description of the positron fraction energy increase is satisfactory, it looks like a constant for B/C at high energies, whereas a decreasing function is expected. With the existing experimental errors, it is difficult to claim a direct contradiction, but more work is apparently needed to improve the model.

5.1.3 Pulsars. Pulsars are rapidly rotating neutron stars, which constantly convert rotation energy into radiation (γ and cosmic rays, including electron–positron pairs of high energy). The energy spectra of electrons and positrons are parameterized as

$$\frac{\mathrm{d}N}{\mathrm{d}E} \sim E^{-\alpha} \exp\left(-\frac{E}{E_{\mathrm{c}}}\right).$$

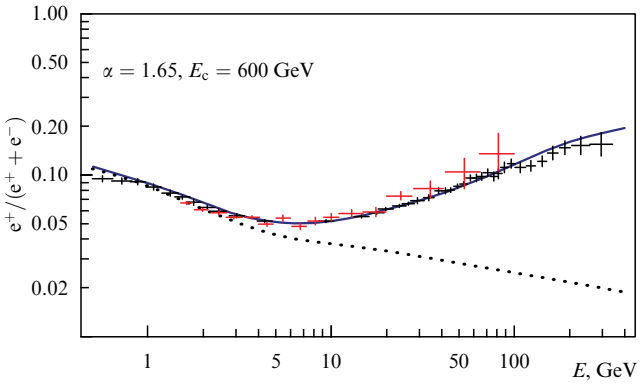

Figure 24. (Color online.) Energy dependence of the positron fraction derived from the combination of all Milky Way pulsars [52]. AMS data (black crosses) and PAMELA data (red crosses).

The parameters have a large uncertainty: $\alpha = 1.5-2.0$ and $E_c = 80-1000$ GeV. In numerical calculations [52], it is assumed that 16% of the total pulsar energy passes to high-energy particles.

The positron fraction energy dependence derived from the combination of all Milky Way pulsars are given in Fig. 24. It shows that the AMS-02 data can be successfully described using reasonably chosen parameters.

In [53], only two pulsars close to us, Geminga and Monogem, were used to describe the AMS data. The result (Fig. 25) is satisfactory.

The most complete analysis of the AMS-02 data was performed in [54]. The spectra of electrons, positrons, and the positron fraction were analyzed in the framework of a model where all astrophysical components that can contribute to the observed fluxes in the available energy range are taken into account. The two main astrophysical sources of primary electrons and positrons are considered: the supernova remnants (SNRs) and pulsars (PWN, Pulsar Wind Nebulae).

The SNRs are assumed to be the main accelerators of charged particles in our Galaxy. The acceleration arises in the expanding shock waves coming from star explosions; power spectra with a high-energy cutoff (2) originate from this mechanism.

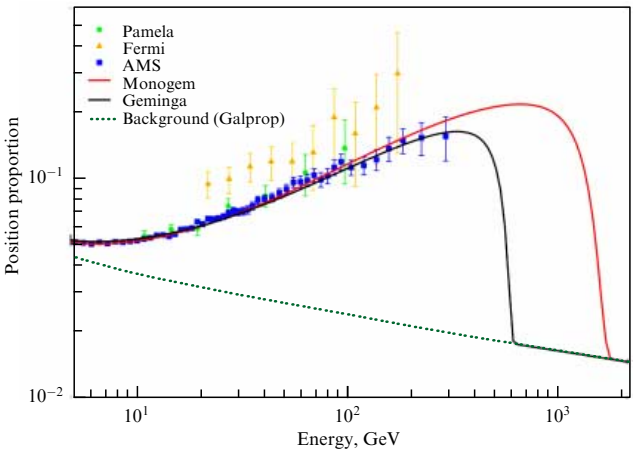

Figure 25. (Color online.) Energy dependence of the positron fraction obtained by taking into account only one pulsar situated closely, Monogem (pink) or Geminga (black) [53].

As regards pulsars, in the region between the shock wave and the star ejecta, a bubble of hot magnetized plasma, called the PWN, is formed. Upon acceleration, particles are captured by the PWN magnetic field and stay there while the PWN exists. The spectrum of accelerated particles is taken in form (2). Because the processes affecting the particles in a pulsar are not known well, there is a large uncertainty in parameters that determine the fluxes of electrons and positrons emitted by pulsars. In the model, the spectra of e^+, e^-, $e^+ + e^-$, and $e^+/(e^+ + e^-)$ are fitted simultaneously. From Fig. 26, where the result is given, we see that the whole complex of lepton spectra is reproduced well by the theoretical model with reasonable parameters. As the authors of [54] pointed out, the spectrum complex can be reproduced by the known astrophysical sources without the introduction of new ones, such as dark matter.

5.1.4 Dark matter. The results described in the preceding section made the dark matter contribution more difficult and less trivial to identify. It is highly desirable to find the spectrum features indicating the dark matter contribution.

We consider several examples of a good description of the AMS-02 data using various scenarios of annihilation and decay of dark matter.

In [55], the experimentally measured positron fraction is explained by the lepton decays of gravitinos. The data are described quite well (Fig. 27a). A similar study was done in [56], where two scenarios of dark matter annihilation were considered as an example. Again, the AMS-02 data are reproduced reasonably well without difficulty (Fig. 27b).

Another example is the description of the positron fraction increase at high energies by ascribing it to the annihilation of the dark matter particle (vino) into leptons [57] (Fig. 27c). As was shown in [58], the high accuracy of AMS-02 data requires a good description of a two-component scenario of decaying dark matter particles (see Fig. 27d).

A combined model, which includes the main astrophysical sources, SNRs and pulsars (PWN), also includes the contributions from practically all scenarios of dark matter with annihilation and particle decay [59]. The remarkable conclusion is that dark matter particles with a mass close to 50 GeV annihilate via the muon channel with a close-to-thermal equilibrium cross section and, after being added to the contribution of pulsars and secondaries, give an exceptionally good fit with the AMS-02 data, a much better fit than in the case of astrophysical contributions only. The result is shown in Fig. 28.

5.1.5 Additional comments. A few additional comments are in order [60].

1. Dark matter with supersymmetric particles annihilating via lepton channels reproduce the AMS-02 data extremely well. However, the annihilation cross sections used in these models are too high, many orders of magnitude greater than the values needed for dark matter if it has been in thermodynamic equilibrium such that the cosmological density expected today is eventually reached.

2. Such large cross sections can violate the unitarity limit $(4\pi/m_\chi^2)(2J+1)$, where J is the angular momentum and m_χ is the mass of the dark matter particle. Only $\mu^+\mu^-$ and $\tau^+\tau^-$ do not violate the unitarity limit, while the b^+b^- and W^+W^- channels obviously violate it.

3. In [61], the study of γ-radiation, including many satellite galaxies of our Milky Way, was performed and the

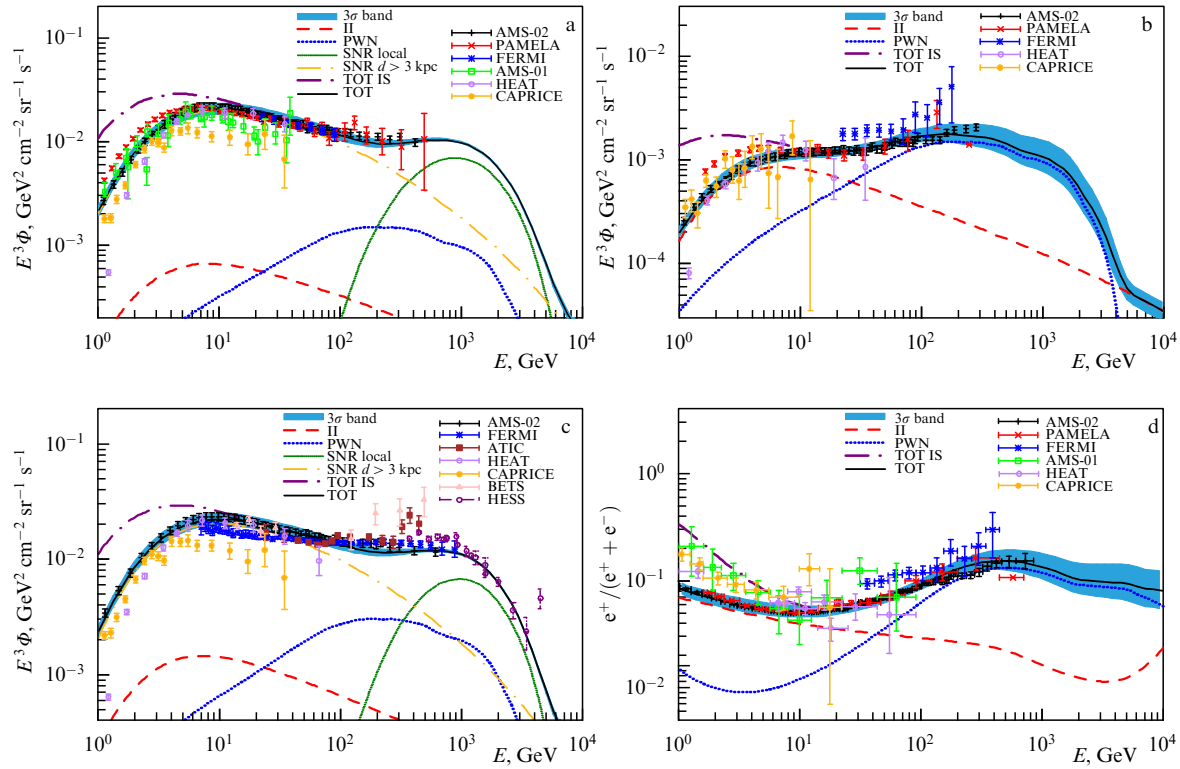

Figure 26. (Color online.) Simultaneous fitting of the spectra of (a) e^-, (b) e^+, and (c) $e^+ + e^-$ obtained in the AMS-02 experiment. The result is shown by the solid line. The contribution of electrons of far (> 3 kpc) SNRs is shown by the yellow dashed-dotted line.The contribution of local SNRs, green dotted line.The contribution of electrons coming from pulsars, blue short dashes. The contribution of secondary electrons and positrons, long red dashes. Also given are data from earlier experiments: Fermi-LAT [38], Pamela [39], Heat [42], Caprice [41], Bets [46], and Hess [36].

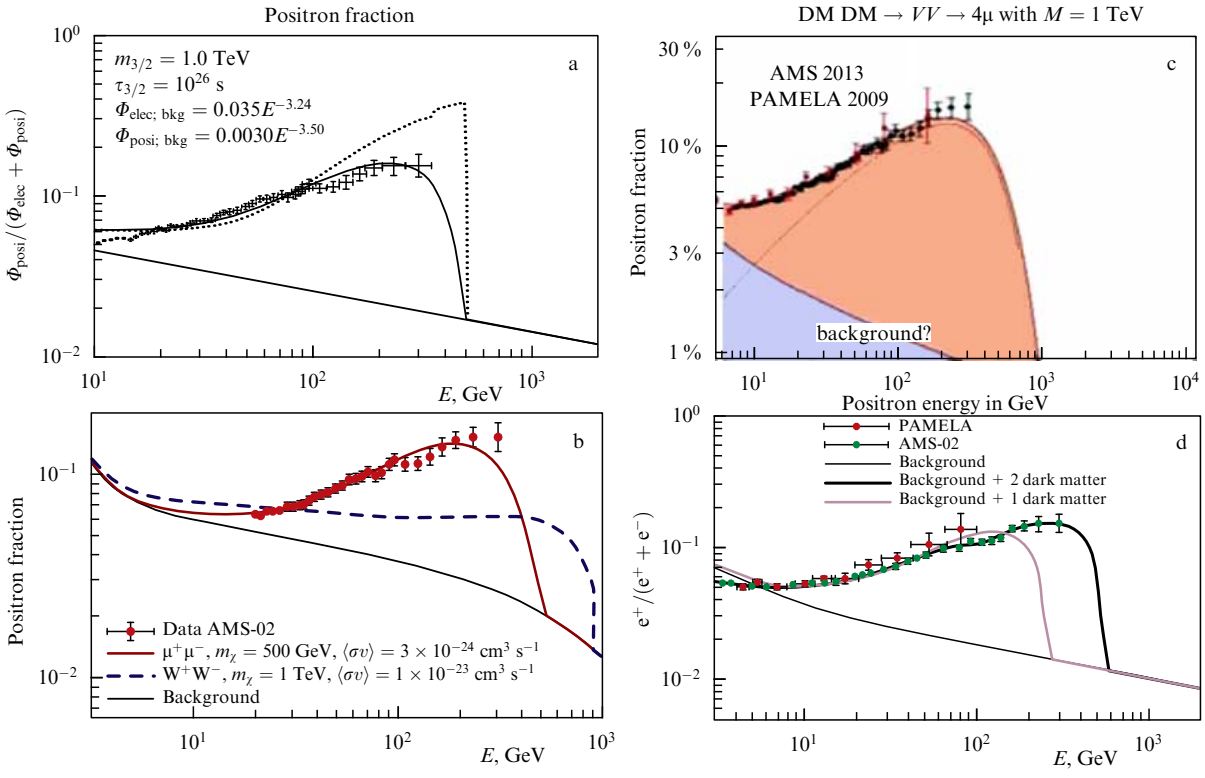

Figure 27. (Color online.) (a) The positron fraction expected from the gravitino decay [55]. (b) Comparison of the AMS data with two scenarios of dark matter annihilation [56]. (c) The fit of the AMS data in the scenario with vino annihilation [57]. (d) AMS data description with decays of two-component dark matter [58].

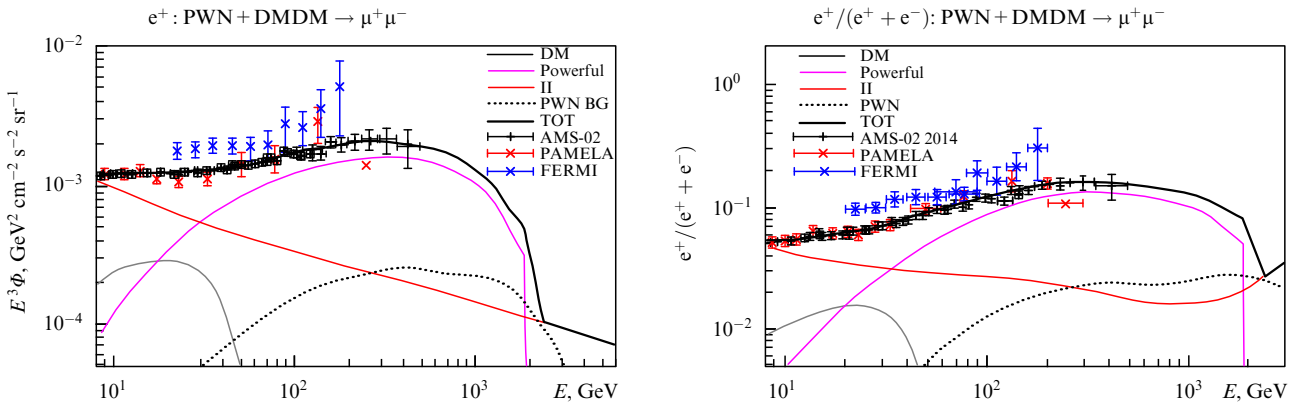

Figure 28. Best fit of the AMS data (e^+ and $e^+/(e^+ + e^-)$) in the combined model that includes astrophysical sources and all scenarios of dark matter with decay and annihilation into leptons [59].

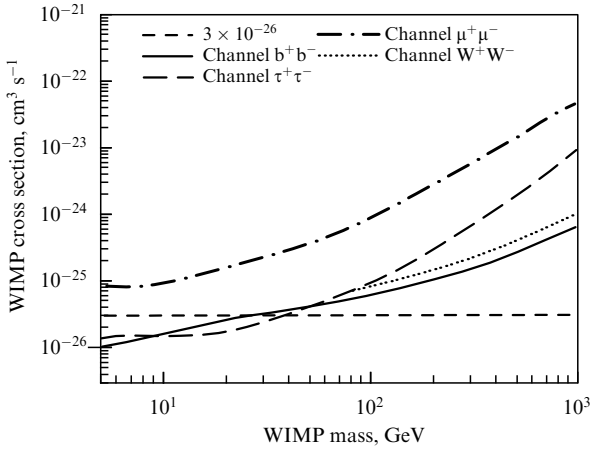

Figure 29. Upper bounds on the dark matter cross section from the analysis of γ-radiation [61].

upper bounds on dark matter annihilation cross sections were obtained (Fig. 29). Although a large uncertainty remains, they ruled out dark matter annihilation up to masses of 27–37 GeV (channel dependent).

5.2 Results on protons and He spectra

Protons are the most abundant cosmic ray component. Being very important for understanding the origin and propagation of cosmic rays, protons have been measured many times over a number of years and even decades. The measurement accuracy has gradually improved but is still not satisfactory for making convincing comparisons and choosing a theoretical model. We compare the AMS data with recent studies.

At high energies, the spectrum becomes harder, the spectral index changes, and model modification is needed. The results of PAMELA indicated the possible existence of a complicated structure in the proton and helium spectra at a few hundred GeV.

The AMS-02 measurements changed the picture dramatically. Figure 30 shows the AMS-02 results for protons [31] and helium [32] in comparison with recent measurements [35, 62–64]. The AMS measurements were made in the energy (rigidity) range 1 GV–1.8 TV (p) and 1.9 GV–3 TV (He) and were based on a sample of 300 mln events of protons and 50 mln He events.

The AMS data on protons and He multiplied by $R^{2.7}$ are shown in Fig. 31. Describing the AMS data in a traditional

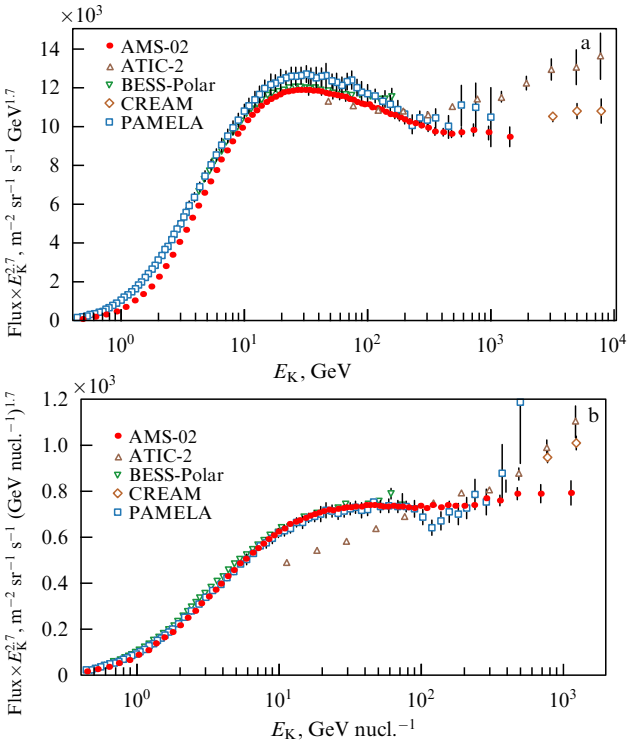

Figure 30. Comparison of AMS (a) proton spectrum and (b) He spectrum with recent measurements.

way with a single power-law function is obviously impossible. For a quantitative estimate, the double power law with a smooth transition of the index γ from lower to higher energies was chosen because it reproduces our data well. The spectrum was fitted by the function (45 GV $< P <$ 18 TV)

$$\Phi = C\left(\frac{R}{45\ \text{GV}}\right)^{\gamma}\left[1+\left(\frac{R}{R_0}\right)^{\Delta\gamma/s}\right]^{s}, \qquad (3)$$

where s is the measure of the transition smoothness of γ from rigidities below the characteristic transition rigidity R_0 to $\gamma + \Delta\gamma$ above R_0. The result of the fit is $\chi^2/\text{NDF} = 25/26$ with the parameters $C = 0.45$, $\gamma = -2.89$, $\Delta\gamma = 0.133$, $s = 0.024$, and $R_0 = 336$ GV (with errors given in [31]) (see Fig. 31). Representing the data with a single power-law function E^{γ} is impossible with 99.9% C.L. For illustration, the dotted curve in Fig. 31 a corresponds to $\Delta\gamma = 0$.

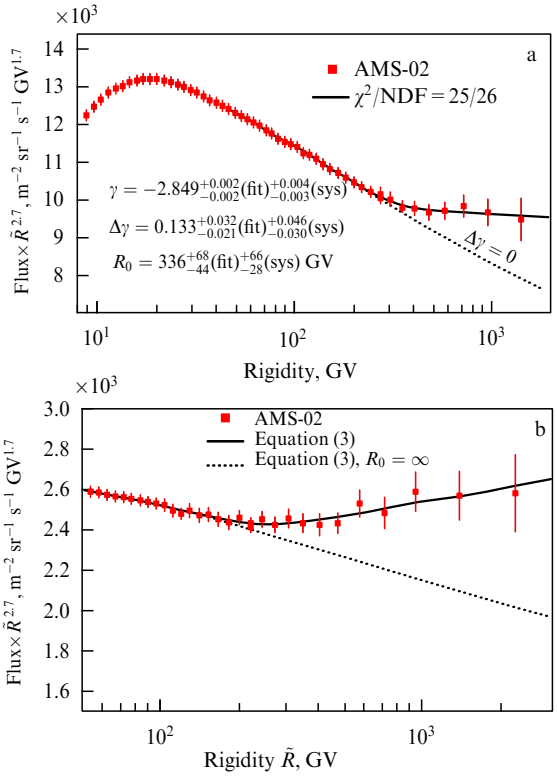

Figure 31. (a) Proton and (b) He spectra approximated by a power-law function. The fluxes are multiplied by $R^{2.7}$.

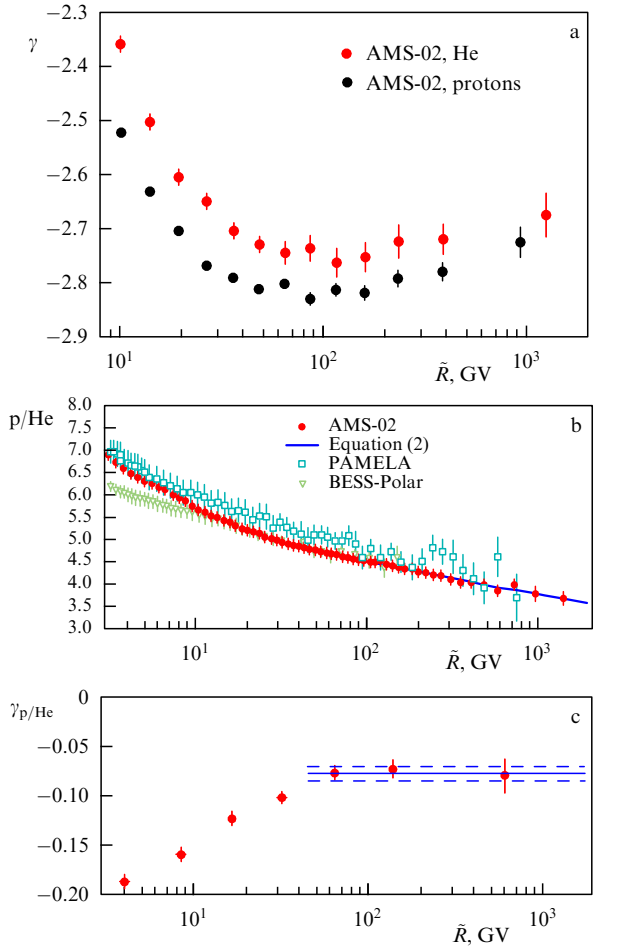

Figure 32. (a) Variation with energy of the proton and helium spectral index; (b) Energy dependence of the proton and helium flux ratio (p/He); (c) Energy dependence of the spectral index of the p/He flux ratio.

We observe the following. Measured by the AMS positron fraction, the spectra of protons and He indicate that the character of the spectrum behavior changes at similar energies. The values of the transition rigidity R_0 for protons ($R_0 = 336 \pm 94$) and He ($R_0 = 245 \pm 48$) are rather close and are also close to the energy of the positron fraction spectrum maximum 275 ± 32 GeV.

In Fig. 32a, the variation of γ for protons and He calculated with the formula

$$\gamma = \frac{\mathrm{d}(\log \Phi)}{\mathrm{d}(\log R)}$$

is given. The index changes with energy, becoming harder above ~ 100 GV.

To understand the proton–helium spectrum difference better, we look at the energy dependence of the ratio of proton and helium fluxes (p/He), which is shown in Fig. 32b, while in Fig. 32c we see the energy dependence of the p/He spectral index $\gamma_{\mathrm{p/He}}$; as can be seen from Fig. 32c, the index increases with energy up to $\cong 45$ GV and then remains constant.

5.3 Antiprotons

Antiprotons are assumed to be secondary particles, i.e., originate from interactions of primaries, produced and accelerated in the source, with the interstellar medium. As shown in [65], the contribution of the secondaries suffices to explain the observed spectrum; no additional components except the standard astrophysical background are needed. A more detailed analysis is performed in [66], where calculation uncertainties have been studied and a conservative estimate of the uncertainties was shown to be 20% in total, up to a maximum of 50%. The result is shown in Fig. 33a, and in Fig. 33b the best fit to the AMS data [33] is given. The main conclusion is confirmed: no antiproton fraction increase is observed; the standard astrophysical background describes the new data quite well.

6. Discussion and conclusions

We summarize. After the first observations in the AMS-01 experiments, the more accurate PAMELA and the recent FERMI-LAT experiments, the precision of AMS-02 data finally confirmed that at high energies the positron fraction grows with energy, although according to the theoretical picture firmly established earlier, it must decrease. The positrons were assumed to be secondaries, i.e., originating from outside the cosmic-ray source; outside the acceleration area, their spectrum was expected to be softer than the electron spectrum. In reality, the spectra of electrons and positrons turned out to be quite different: the positron spectrum is harder, with the spectrum index $\gamma \cong -2.86$, whereas $\gamma \cong -3$ for electrons. This picture corresponds more to the situation where electrons are secondaries and positrons are primaries, i.e., accelerated in the source. To make the picture even more confusing, we mention the decreasing spectrum of the B/C ratio as expected in the accepted picture. Reconciling the B/C behavior with positrons has so far been impossible. After the discovery of the unexpected positron behavior, a number of models appeared predicting a similar increase in the antiproton/proton ratio.

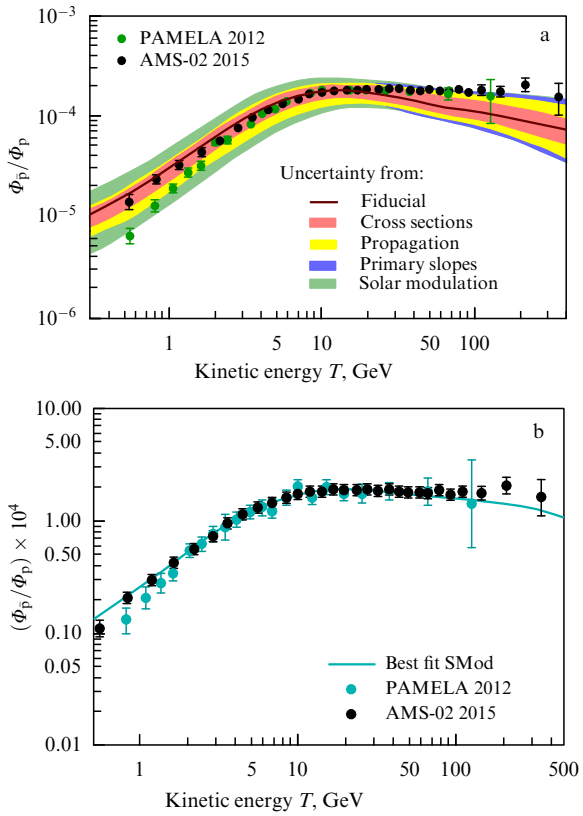

Figure 33. (Color online.) (a) Contribution of different uncertainties to the estimation of the astrophysical background [66]. (b) The best fit to the AMS data.

But the observations show no increase in antiprotons, and this makes it even more difficult to make the whole picture self-consistent.

One of the major objectives of the AMS physics program is the observation of dark matter in its nongravitational manifestations. Now we understand that with annihilation and/or decays of neutralinos into lepton channels, we are able to explain the observed features in positrons and electrons quantitatively, with a good χ^2. The description becomes even better if we add astrophysical sources such as SNR and pulsars to dark matter. Under these conditions, we can identify dark matter if characteristic features are observed in the energy spectrum. For example, the neutralino contribution is expected to sharply drop outside the region that corresponds to the neutralino mass.

The author is grateful to Andrei Kunin, Vasily Plyaskin, and Vitaly Shutko for reading the manuscript and the valuable comments. The author is also thankful to Samuel Ting for his continuous support.

References

1. Ahlen S et al. *Nucl. Instrum. Meth. Phys. Res. A* **350** 351 (1994)
2. Olive K A et al. (Particle Data Group) *Chin. Phys. C* **38** 090001 (2014)
3. Dolgov A D *Phys. Rep.* **222** 309 (1992)
4. Jungman G, Kamionkowski M, Griest K *Phys. Rep.* **267** 195 (1996)
5. Ting S *Nucl. Phys. B Proc. Suppl.* **243** 12 (2013); Chung C H et al. (The AMS Collab.) "AMS on ISS Construction of a particle physics detector on the International Space Station", http://www-ekp.physik.uni-karlsruhe.de/~deboer/html/Forschung/AMS.pdf, unpublished (2007)
6. Kounine A *Int. J. Mod. Phys. E* **21** 1230005 (2012)
7. Aguilar M et al. (AMS Collab.) *Phys. Rep.* **366** 331 (2002)
8. Pauluzzi M *Nucl. Instrum. Meth. Phys. Res. A* **473** 67 (2001)
9. Casadei D et al. *Nucl. Phys. B Proc. Suppl.* **113** 233 (2002); astro-ph/0206021; Alvisi D et al. *Nucl. Instrum. Meth. Phys. Res. A* **437** 212 (1999)
10. von Doetinchem Ph et al. *Nucl. Phys. B Proc. Suppl.* **197** 15 (2009); arXiv:0811.4314
11. Galaktionov Yu V *Rep. Prog. Phys.* **65** 1243 (2002)
12. Alcaraz J et al. (AMS Collab.) *Phys. Lett. B* **461** 387 (1999)
13. Alcaraz J et al. (AMS Collab.) *Phys. Lett. B* **472** 215 (2000)
14. Plyaskin V *Astropart. Phys.* **30** 18 (2008)
15. Alcaraz J et al. (AMS Collab.) *Phys. Lett. B* **484** 10 (2000)
16. Aguilar M (AMS-01 Collab.) *Phys. Lett. B* **646** 145 (2007)
17. Alcaraz J et al. (AMS Collab.) *Phys. Lett. B* **494** 193 (2000)
18. Alcaraz J et al. (AMS Collab.) *Phys. Lett. B* **490** 27 (2000)
19. Blau B et al. *IEEE Trans. Appl. Supercond.* **12** 345 (2002)
20. Pohl M, arXiv:1508.07759
21. v. Deutinchem P et al. *Nucl. Instrum. Meth. Phys. Res. A* **558** 526 (2006); astro-ph/0608641
22. Casaus J *Nucl. Phys. B Proc. Suppl.* **113** 147 (2002)
23. Cervelli F et al. *Nucl. Instrum. Meth. Phys. Res. A* **490** 132 (2002)
24. Roe B P et al. *Nucl. Instrum. Meth. Phys. Res. A* **543** 577 (2005)
25. Basara L, PhD Thesis (Grenoble: École Doctorale Physique Grenoble, Laboratoire d'Annecy-le-Vieux de Physique des Particules, 2014)
26. Gilmore D G *Satellite Thermal Control Handbook* (El Segundo, Calif.: Aerospace Corp. Press, 1994)
27. Aguilar M et al. (AMS Collab.) *Phys. Rev. Lett.* **110** 141102 (2013)
28. Accardo L et al. (AMS Collab.) *Phys. Rev. Lett.* **113** 121101 (2014)
29. Aguilar M et al. (AMS Collab.) *Phys. Rev. Lett.* **113** 221102 (2014)
30. Aguilar M et al. (AMS Collab.) *Phys. Rev. Lett.* **113** 121102 (2014)
31. Aguilar M et al. (AMS Collab.) *Phys. Rev. Lett.* **114** 171103 (2015)
32. Aguilar M et al. (AMS Collab.) *Phys. Rev. Lett.* **115** 211101 (2015)
33. Aguilar M et al. (AMS Collab.) *Phys. Rev. Lett.* **117** 091103 (2016)
34. Moskalenko I V, Strong A W *Astrophys. J.* **493** 694 (1998)
35. Panov A D et al. *Bull. Russ. Acad. Sci. Phys.* **73** 564 (2009); *Izv. Ross. Akad. Nauk Ser. Fiz.* **73** 602 (2009)
36. Aharonian F et al. (H.E.S.S. Collab.) *Phys. Rev. Lett.* **101** 261104 (2008)
37. Borla Tridon D et al., in *32nd Intern. Cosmic Ray Conf., Beijing 2011*; https://doi.org/10.7529/ICRC2011/V06/0680; arXiv:1110.4008
38. Ackermann M et al. (Fermi LAT Collab.) *Phys. Rev. Lett.* **108** 011103 (2012)
39. Adriani O et al. *Nature* **458** 607 (2009)
40. Grimani C et al. *Astron. Astrophys.* **392** 287 (2002)
41. Boezio M et al. *Adv. Space Res.* **27** 669 (2001)
42. DuVernois M A et al. *Astrophys. J.* **559** 296 (2001)
43. Golden R L et al. *Astrophys. J.* **457** L103 (1996)
44. Torii S et al. *Astrophys. J.* **559** 973 (2001)
45. Chang J et al. *Nature* **456** 362 (2008)
46. Yoshida K et al. *Adv. Space Res.* **42** 1670 (2008)
47. Blasi P *Phys. Rev. Lett.* **103** 051104 (2009)
48. Fujita Y et al. *Phys. Rev. D* **80** 063003 (2009)
49. Mertsch P, Sarkar S *Phys. Rev. D* **90** 061301(R) (2014)
50. Cholis I, Hooper D *Phys. Rev. D* **89** 043013 (2014)
51. Cowsik R, Burch B, Madziwa-Nussinov T *Astrophys. J.* **786** 124 (2014)
52. Cholis I, Hooper D *Phys. Rev. D* **88** 023013 (2013); arXiv:1304.1840
53. Linden T, Profumo S *Astrophys. J.* **772** 18 (2013); arXiv:1304.1791
54. Di Mauro M et al. *JCAP* (04) 006 (2014); arXiv:1402.0321
55. Ibe M et al. *J. High Energ. Phys.* **2013** (08) 29 (2013); arXiv:1304.1483
56. Kopp J *Phys. Rev. D* **88** 076013 (2013); arXiv:1304.1184
57. Cirelli M *Nucl. Phys. B* **813** 1 (2009); arXiv:0809.2409
58. Kajiyama Y, Okada H, Toma T *Eur. Phys. J. C* **74** 2722 (2014); arXiv:1304.2680
59. Di Mauro M et al. *JCAP* (05) 031 (2016); arXiv:1507.07001
60. Spanos V C, arXiv:1312.7841
61. Ackermann M et al. (The Fermi-LAT Collab.) *Phys. Rev. Lett.* **107** 241302 (2011); arXiv:1108.3546
62. Abe K et al. *Phys. Rev. Lett.* **108** 051102 (2012)
63. Yoon Y S et al. *Astrophys. J.* **728** 122 (2011)
64. Adriani O et al. *Science* **332** 69 (2011)
65. Donato F et al. *Phys. Rev. Lett.* **102** 071301 (2009)
66. Giesen G et al. *JCAP* (09) 023 (2015); arXiv:1504.04276